Draft version December 20, 2016

Preprint typeset using LaTeX style AASTeX6 v. 1.0

arXiv:1612.05655v1 [astro-ph.GA] 16 Dec 2016

THE RELATION BETWEEN GLOBULAR CLUSTER SYSTEMS AND SUPERMASSIVE BLACK HOLES IN SPIRAL GALAXIES. THE CASE STUDY OF NGC 4258.

Rosa A. González-López lira[1,2], Luis Lomelí-Núñez[1], Karla Álamo-Martínez[3], Yasna Órdenes-Briceño[3], Laurent Loinard[1], Iskren Y. Georgiev[4], Roberto P. Muñoz[3], Thomas H. Puzia[3], Gustavo Bruzual A.[1], Stephen Gwyn[5]

1 Instituto de Radioastronomia y Astrofisica, UNAM, Campus Morelia, Michoacan, Mexico, C.P. 58089

2 Argelander Institut für Astronomie, Universität Bonn, Auf dem Hügel 71, D-53121 Bonn, Germany

3 Instituto de Astrofísica, Pontificia Universidad Católica de Chile, Av. Vicuña Mackenna 4860, 7820436 Macul, Santiago, Chile

4 Max-Planck Institut für Astronomie, Königstuhl 17, D-69117 Heidelberg, Germany

and

5 Herzberg Institute of Astrophysics, National Research Council of Canada, Victoria, BC V9E 2E7, Canada

ABSTRACT

We aim to explore the relationship between globular cluster total number, $N_{\rm GC}$, and central black hole mass, $M_\bullet$, in spiral galaxies, and compare it with that recently re-

ported for ellipticals. We present results for the Sbc galaxy NGC 4258, from Canada France Hawaii Telescope data. Thanks to water masers with Keplerian rotation in a circumnuclear disk, NGC 4258 has the most precisely measured extragalactic distance and supermassive black hole mass to date. The globular cluster (GC) candidate selection is based on the $(u^* - i')$ vs. $(i' - K_s)$ diagram, which is a superb tool to distinguish GCs from foreground stars, background galaxies, and young stellar clusters, and hence can provide the best number counts of GCs from photometry alone, virtually free of contamination, even if the galaxy is not completely edge-on. The mean optical and optical-near infrared colors of the clusters are consistent with those of the Milky Way and M 31, after extinction is taken into account. We directly identify 39 GC candidates; after completeness correction, GC luminosity function extrapolation and correction for spatial coverage, we calculate a total $N_{\rm GC} = 144 \pm 31^{+38}_{-36}$ (random and systematic uncertainties, respectively). We have thus increased to 6 the sample of spiral galaxies with measurements of both $M_\bullet$ and $N_{\rm GC}$. NGC 4258 has a specific frequency $S_{\rm N} = 0.4 \pm 0.1$ (random uncertainty), and is consistent within 2σ with the $N_{\rm GC}$ vs. $M_\bullet$ correlation followed by elliptical galaxies. The Milky Way continues to be the only spiral that deviates significantly from the relation.

Keywords: black hole physics — galaxies: spiral — galaxies: formation — galaxies: evolution — galaxies: star clusters: general — globular clusters: general — galaxies: individual (NGC 4258)

1. INTRODUCTION

It is virtually certain that all massive galaxies contain central black holes. In spheroidal systems, the masses of these black holes, $M_\bullet$, correlate with the galaxy bulge luminosity (the $M_\bullet$–$L_{\rm bulge}$ relation,

e.g., Kormendy 1993; Kormendy & Richstone 1995; Magorrian et al. 1998; Kormendy & Gebhardt 2001; Marconi & Hunt 2003; Gültekin et al. 2009), mass (e.g., Dressler 1989; Magorrian et al. 1998; Laor 2001; McLure & Dunlop 2002; Marconi & Hunt 2003; Häring & Rix 2004), and stellar velocity dispersion (the $M_\bullet$–σ_* relation, e.g., Ferrarese & Merritt 2000; Gebhardt et al. 2000; Tremaine et al. 2002; Gültekin et al. 2009). Spitler & Forbes (2009) also find a relation between black hole mass and dark matter halo mass, as inferred from globular cluster system total mass. Such correlations could be the result of central black hole and spheroid evolution. Exploring the limits and deviations from these correlations can help illuminate the different evolutionary processes that influence the growth of galaxies and their black holes (e.g., McConnell et al. 2011).

It is unclear whether spiral galaxies fall on these relations. At least in the case of the $M_\bullet$–σ_* and $M_\bullet$–$M_{\rm bulge}$ relations, although they exist for spirals, they appear to have larger scatter than for ellipticals. Also, some barred spirals and pseudobulges can be up to one order of magnitude offset in the $M_\bullet$–σ_* diagram, with black holes that are too small for the velocity dispersion of the bulge (e.g., Hu 2008; Greene et al. 2008; Gadotti & Kauffmann 2009; Greene et al. 2010). The scatter could be caused by measurement uncertainties, but it could also be intrinsic, e.g., if black hole growth is stochastic to some extent, depending on inward gas flow and galaxy-to-galaxy differences in gas accretion rates. Graham (2012a,b) suggests that the $M_\bullet$–$L_{\rm bulge}$ and $M_\bullet$–$M_{\rm bulge}$ relations might be broken or curved for galaxies with $M_B > -20.5$ mag, even if they have real bulges. Läsker et al. (2016) also find hints that a galaxy's low mass may be more of a determinant than the absence of a classical bulge.

Interestingly, Burkert & Tremaine (2010) and, with more data, Harris & Harris (2011); Harris et al. (2014) have shown that the central black hole mass of elliptical galaxies increases almost exactly proportionally to the total number of their globular clusters, $N_{\rm GC}$. The correlation can be expressed as $N_{\rm GC} \propto M_\bullet^{1.02\pm0.10}$, spans over 3 orders of magnitude, and is tighter than the $M_\bullet - \sigma_*$ relation.

The most likely link between $N_{\rm GC}$ and $M_\bullet$ is the galaxy potential well/binding energy ($M_*\sigma_*^2$, where M_* is the bulge stellar mass), with which both quantities are correlated (e.g., Snyder et al. 2011; Rhode 2012). However, given the extremely disparate scales of both components, the tightness of the correlation is intriguing and has been intensely explored. Kormendy & Ho (2013) review the status of these endeavors. For example, Harris et al. (2013) find that $N_{\rm GC} \propto (R_e\sigma_e)^{1.3}$, with R_e the effective radius of the galaxy light profile (bulge+disk) and σ_e the velocity dispersion at the half-light radius. On the other hand, while Sadoun & Colin (2012) show that the correlation between $M_\bullet$ and the velocity dispersion of globular cluster *systems* as a whole is tighter for red than for blue GCs in a sample of 12 galaxies, Pota et al. (2013) do not find a significantly smaller scatter in the correlation for either one of the blue and red subsystems in an enlarged sample of 21 galaxies with better $M_\bullet$ measurements. Regarding $N_{\rm GC}$, Rhode (2012) finds that the number of blue GCs correlates better with $M_\bullet$. Also, for the few spirals in her sample, Rhode (2012) gets a better correlation of $N_{\rm GC}$ with bulge light than with total light; however, the correlation of $N_{\rm GC}$ is much tighter with total galaxy stellar mass than with bulge mass. de Souza et al. (2015) perform an exhaustive analysis of the $N_{\rm GC}$ vs. $M_\bullet$ relation from the point of view of Bayesian statistics; they conclude that black hole mass is a good predictor of total number of GCs.

The $N_{\rm GC}$ vs. $M_\bullet$ correlation could be rooted in the initial conditions of galaxy formation or in the process of galaxy assembly, and the scaling relations between different galaxy components could give clues about which origin is more likely.

Precisely because of the 10 orders of magnitude that separate the spatial scales of supermassive black holes (SMBHs) and globular cluster systems, a direct causal link has been often quickly dismissed with the argument that bigger galaxies should have more of everything. Nontheless, possible causal relations have been proposed. Harris et al. (2014) offer a review of them, namely: star (and hence GC) formation driven by AGN jets (e.g., Silk & Rees 1998; Fabian 2012); BH growth through the

cannibalization of GCs (e.g., Capuzzo-Dolcetta & Donnarumma 2001; Capuzzo-Dolcetta & Vicari 2005; Capuzzo-Dolcetta & Mastrobuono-Battisti 2009; Gnedin et al. 2014), especially efficient if all GCs contain intermediate mass BHs (Jalali et al. 2012). Another mechanism for the establishment of scaling relations would be the statistical convergence process of galaxy characteristics through hierarchical galaxy formation (Peng 2007; Jahnke & Macciò 2011).

Besides the issue of its origin, a well understood $N_{\rm GC}$ – $M_\bullet$ correlation could be useful as a tool to estimate masses of inactive black holes, that would otherwise be hard to measure.

Before the present work, there were only 5 spiral galaxies with precise measurements of both $N_{\rm GC}$ and $M_\bullet$: the Milky Way (MW, Sbc), M 104 (Sa), M 81 (Sab), M 31 (Sb) and NGC 253 (Sc). All of them, with the notable exception of the MW, fall right on the $N_{\rm GC} - M_\bullet$ correlation for ellipticals. Our Galaxy has a black hole that is about 1 order of magnitude lighter than expected from its $N_{\rm GC}$.

Spirals have both less massive black holes and less rich GC systems than ellipticals and lenticulars, and hence have been studied much less frequently than early type galaxies. Concerning in particular GCs, internal extinction and potential confusion with stars and star clusters in their galactic disks have in general further limited studies in spirals to galaxies seen edge-on.

In what follows, we present new measurements and analysis of the globular cluster system of the Sbc galaxy NGC 4258 (M 106). Thanks to water masers in a disk orbiting its nucleus, its absolute distance has been derived directly by geometric means (Herrnstein et al. 1999). NGC 4258 hence has the most precisely measured extragalactic distance and SMBH mass to date, i.e., 7.60±0.17±0.15 Mpc (formal fitting and systematic errors, respectively) and $(4.00\pm0.09)\times10^7 M_\odot$ (Humphreys et al. 2013). In spite of being the archaetypical megamaser galaxy, however, NGC 4258 has a classical bulge, unlike most other megamaser galaxies (Läsker et al. 2014, 2016); it also falls on the $M_\bullet$–$L_{\rm bulge}$ and $M_\bullet$–$M_{\rm bulge}$ for ellipticals (Sani et al. 2011; Läsker et al. 2016). With an inclination to the line of sight of 67° (de Vaucouleurs et al. 1991), NGC 4258 is not an edge-on galaxy. Ours is the first

application of the $(u^* - i')$ vs. $(i' - K_s)$ diagram technique ($u^*i'K_s$ hereafter; Muñoz et al. 2014) to a spiral galaxy. We will show that with this procedure one can get the *best* total number counts of GCs from photometry alone that are virtually free of contamination from foreground stars and background galaxies, *without the need to obtain radial velocity measurements*. In addition, the $u^*i'K_s$ plot can easily weed out young star clusters in a spiral disk. We will quantify the efficiency of the $u^*i'K_s$ diagram to produce a clean sample of GC candidates (GCCs) in a disk galaxy.

2. DATA

All data for the present work were obtained with the Canada-France-Hawaii-Telescope (CFHT). The optical images of NGC 4258 are all archival, and were acquired with MegaCam (Boulade et al. 2003). MegaCam has 36 2048×4612 CCD42-90 detectors operating at -120° C, and sensitive from 3700 to 9000 $\mathring{A}$; read-out-noise and gain are, respectively, < 5 e$^-$ pixel^{-1} and ~ 1.62 e$^-$ ADU^{-1}. The detectors are arranged in a 9×4 mosaic with 13″ small gaps between CCD columns, and 80″ large gaps between CCD rows. The field-of-view (FOV) of MegaCam is $0.^\circ96 \times 0.^\circ94$, with a plate scale of $0.''186$ pixel^{-1}.

Images were originally secured through programs 08BH55, 09AH42, 09AH98, 09BH95 (P.I. E. Magnier, u^*-band); 09AC04 (P.I. R. Läsker, u^* and i' filters); 10AT01 (P.I. C. Ngeow, g', r', and i' bands), and 11AC08 (P.I. G. Harris, g' and i' data).

Before archiving, MegaCam images are "detrended", i.e., corrected for the instrumental response (bad pixel removal, overscan and bias corrections, and flat-fielding, plus defringing for the i' and z' bands) with the Elixir software (Magnier & Cuillandre 2004). Elixir also provides a global astrometric calibration with an accuracy of $0.''5 - 1.''0$, and a photometric calibration with a uniform zero point whose internal accuracy is better than 1% for the entire image.

To make the final u^*, g', r', and i' mosaics of NGC 4258, individual images were combined with

the MegaPipe pipeline (Gwyn 2008). MegaPipe groups the images by passband; resamples them to correct the geometric distortion of the MegaCam focal plane; recalibrates the astrometry to achieve internal and external accuracies of 0.″04 and 0.″15, respectively; recalibrates the photometry, mainly to account for modifications made to the Elixir pipeline in different epochs, with an output accuracy of 0.03 mag; and finally stacks them.

The K_s-band images of NGC 4258 were acquired on 2013 March 27 UT, through proposal 13AC98 (P.I. R. González-Lópezlira), with the Wide-field InfraRed Camera (WIRCam; Puget et al. 2004). WIRCam has four 2048×2048 HAWAII2-RG HgCdTe detectors, cooled cryogenically to $\sim 80°$ K, and sensitive at 0.9-2.4 μm; read-out-noise and gain are, respectively, 30 e^- pixel^{-1} and 3.7 e^- ADU^{-1}. The detectors are organized in a 2×2 mosaic with 45″ interchip gaps. The FOV of the WIRCam is $\sim 21' \times 21'$, with a plate scale of 0.″307 pixel^{-1}.

We obtained 10×20 s individual K_s exposures of NGC 4258. The telescope pointing was dithered in an approximately circular pattern with a radius $\sim$ 1.′6. Because of the galaxy large diameter compared to WIRCam's FOV ($R_{25} = 9.'3$; de Vaucouleurs et al. 1991), separate 10×20 s sky frames were taken 2.°1 away, with the same circular pattern, using the following target(T)-sky(S) sequence: STTSSTTSS...TTS. Figure 1 displays the sky-coverage map for the galaxy overlaid on our final K_s-band mosaic; number of overlapping exposures increases with color intensity, up to a maximum of 10.

In the case of WIRCam images, detrending is performed by the I'iwi pipeline.[1] Detrending includes saturated pixel flagging; non-linearity correction; bias (reference pixel) and dark current subtraction; flat-fielding, and bad pixel masking. I'iwi also gives a global astrometric calibration with an accuracy of 0.″5 – 0.″8; the photometric zero point however, is different for each of the WIRCam detectors at

[1] http://www.cfht.hawaii.edu/Instruments/Imaging/WIRCam/IiwiVersion1Doc.html.

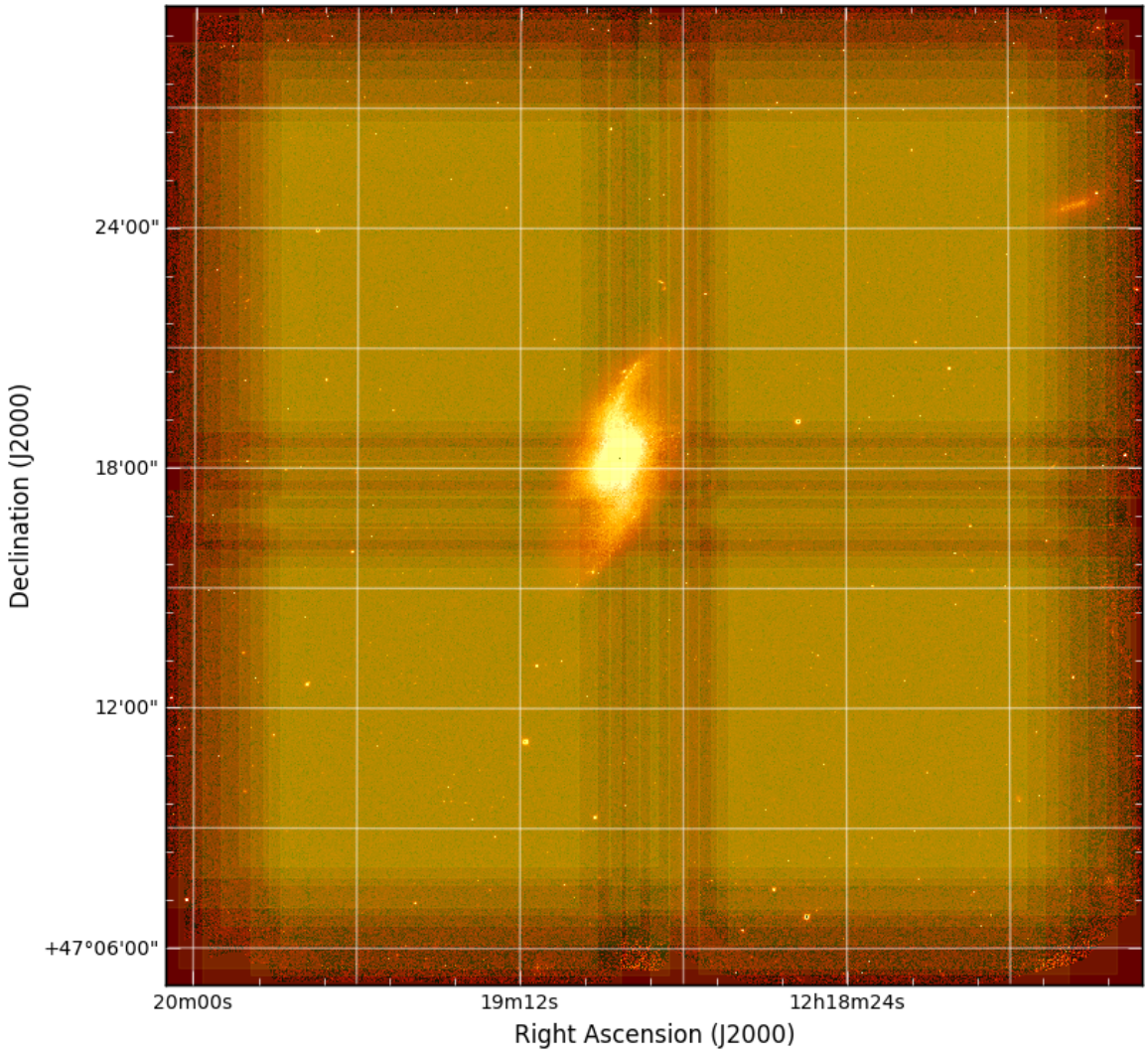

Figure 1. NGC 4258 coverage map on our final K_s-band image. Number of overlapping exposures increases with color intensity, up to 10. *This figure was made with the Kapteyn software package* (Terlouw & Vogelaar 2015).

the end of the I'iwi processing.

To produce the final K_s-band mosaic of NGC 4258, individual images were sky-subtracted and combined with the WIRwolf pipeline (Gwyn 2014). Like MegaPipe, WIRwolf resamples the individual images; recalibrates their astrometry to a typical internal accuracy of $0\farcs1$; provides a uniform zero point for the four detectors; and stacks them.

Both MegaPrime and WIRwolf output images with photometry in the AB system (Oke 1974), with zero points $zp = 30$. Given its smaller FOV and significantly shorter exposure time, all our analysis

Table 1. NGC 4258 Observation Log

Filter	λ^a_{cen}	FWHM[b]	Exposure	Camera	Pixel size	Program	Date
			s		$''$		UT
u^*	3793 Å	654 Å	13360	Megacam	0.186	08BH55	2008 December 22, 23
						09AC04	2009 February 18
						09AH42	2009 March 27, 30
						09AH98	2009 April 19
						09BH95	2009 December 11
g'	4872 Å	1434 Å	10400	Megacam	0.186	10AT01	2010 June 11, 12; July 7, 8
						11AC08	2011 March 1
r'	6276 Å	1219 Å	3500	Megacam	0.186	10AT01	2010 June 16; July 8, 12
i'	7615 Å	1571 Å	8080	Megacam	0.186	09AC04	2009 February 26
						10AT01	2010 June 10, 12, 13, 15; July 8,12
K_s	2.15 μm	0.33 μm	200	WIRCam	0.307	13AC98	2013 March 27

NOTE— [a]The central wavelength between the two points defining FWMH (http://svo2.cab.inta-csic.es/svo/theory/fps3/index.php?id=CFHT/).

[b] *Ibid.*

will be limited by the K_s-band image of NGC 4258.

Table 1 gives a summary of the NGC 4258 observations.

3. DETECTION AND PHOTOMETRY

Source detection and photometric measurements in all the stacked images were carried out with SExtractor (Bertin & Arnouts 1996) and PSFEx (Bertin 2011). PSFEx employs point sources detected in a first pass of SExtractor to build a point-spread function (PSF) model that SExtractor

can then apply in a second pass to obtain PSF magnitudes of sources. We used versions 2.8.6 (first pass) and 2.19.4 (second pass) of SExtractor, and PSFEx version 3.9.1.

Although PSFEx can select automatically sources (PSF stars) to build the model PSF, instead we chose adequate stars manually, carefully discarding saturated, extended, and spurious sources. The selection is based on the brightness vs. compactness parameter space, as measured by SExtractor parameters MAG_AUTO and FLUX_RADIUS,[2] respectively. The plot is shown in Figure 2 for all passbands, with PSF stars highlighted as red dots. The selection criteria, as well as the number of detected (in both the first, SEx 1, and second, SEx 2, runs of SExtractor) and chosen points at each wavelength, are listed in Table 2. In order for PSFEx to work, one needs to have VIGNET as an output parameter in a previous run of SExtractor. VIGNET(width,height) specifies the size in pixels of the region around each PSF star that will be considered; one also needs to instruct SExtractor to perform photometry in a circular aperture with a diameter PHOT_APERTURES of the same size. These size and aperture must be enough to include most of the stellar flux, but as small as possible to minimize the risk of contamination from other objects. The VIGNET (and hence aperture) sizes are likewise shown in Table 2.

The spatial variations of the PSF were modeled with polynomials of degree 4 for the optical mosaics, and of degree 2 for the smaller K_s image. When running with a PSF model, SExtractor can measure PSF magnitudes (MAG_PSF) and produce another, very useful, estimator of shape, called SPREAD_MODEL. The SPREAD_MODEL value for each object results from the comparison be-

[2] FLUX_RADIUS estimates the radius of the circle centered on the light barycenter that encloses about half of the total flux. 2×FLUX_RADIUS equals the FWHM for a Gaussian profile, but for seeing-limited images 2×FLUX_RADIUS $\sim$ 1.05 – 1.1 FWHM; for profiles with a significant fraction of flux in the wings, the difference can be much larger (http://www.astromatic.net/forum/showthread.php?tid=516). MAG_AUTO is a Kron-like (Kron 1980) elliptical aperture magnitude (http://terapix.iap.fr/article.php?id_article=628). The radius, ellipticity, and position angle of the aperture are defined from the first and second moments of the object's light profile (Bertin & Arnouts 1996).

Table 2. PSFEx Parameters

		FLUX_RADIUS		MAG_AUTO		N sources	
Filter	VIGNET	Min	Max	Min	Max	Total	PSF stars
	pixel × pixel	pixel		mag		SEx 1/ SEx 2	
u^*	20 × 20	2.35	2.60	17.0	22.5	132183/132276	915
g'	20 × 20	2.35	2.60	18.5	22.5	233053/232304	1247
r'	20 × 20	2.40	2.70	17.0	22.0	122867/122867	1855
i'	20 × 20	1.80	2.20	18.0	22.0	218200/218142	2173
K_s	15 × 15	1.45	1.70	16.0	19.5	9276/9272	145

tween its best fitting PSF, and the convolution of such PSF with an exponential disk with scale length $\mathrm{FWHM_{PSF}}/16.$, where $\mathrm{FWHM_{PSF}}$ is the full width at half max of the same PSF (Desai et al. 2012).

4. COMPLETENESS

Completeness tests were only performed on the K_s-band data; this is the smallest and shallowest image and in fact sets our object detection limit. In order to determine the GC detection completeness as a function of magnitude, $\sim$ 320,000 artificial point sources were generated based on the PSF model, in the interval 17 mag $< m_{Ks} <$ 23 mag, and with a uniform, or box-shaped, magnitude distribution. Due to the WIRCam pixel size, $0\farcs307$ or $\gtrsim$ 11 pc at the distance of NGC 4258, GCCs are unresolved in the K_s-band image.

The artificial objects were added only $\sim$1000 at a time (we call this one simulation), in order to prevent creating artificial crowding. The K_s-band image of NGC 4258 was divided into square bins 155 pixels on the side, and only one artificial object was added in each bin. The positions of the

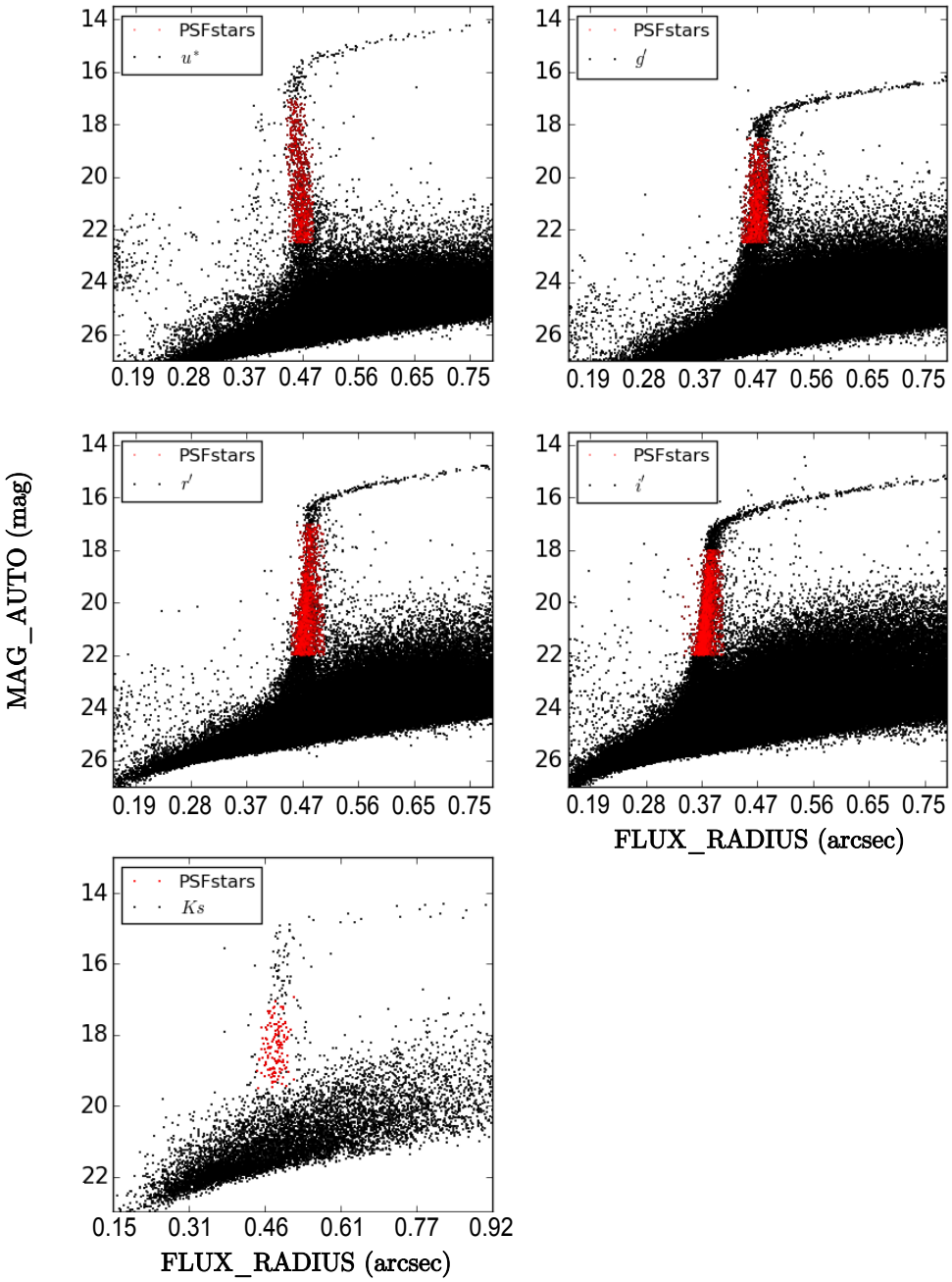

Figure 2. PSF star selection. Plots of MAG_AUTO vs. FLUX_RADIUS for the u^* (top left), g' (top right), r' (middle left), i' (middle right), and K_s (bottom left) bands. Point sources are located in the vertical columns of dots; saturated sources lie in the plume at roughly constant MAG_AUTO; the cloud at faint magnitudes contains both extended and spurious sources, like cosmic rays. Selected PSF stars are shown as red dots.

added sources were random, but assigned avoiding overlapping with other artificial objects or with real sources identified by the SExtractor segmentation map. To reach 320,000 artificial sources for the whole image, we carried out 160 simulation pairs, i.e., we produced 320 images, each one with $\sim$ 1000 added sources, but there were only 160 different sets of positions. The artificial objects in a simulation pair had the same positions, but their magnitudes were different in each of the two members of the pair.

SExtractor was then run on each one of the 320 simulated images, with the same parameters used for the original K_s-band image of NGC 4258, and the recovered artificial sources were identified by cross-matching the positions of all detections with the known input coordinates of the added objects. Aside from non-detections, objects with SExtractor output parameter FLAGS $\neq 0$ were eliminated.[3] The requirement FLAGS=0 excludes artificial objects falling on top of other artificial or real sources, and hence discards preferentially added objects in crowded regions. The criterion FLAGS=0 was also applied in the selection of true sources (see Section 5).

Given that NGC 4258 is a spiral galaxy, and not edge-on, it was of particular interest to quantify the effect of the disk on source detection. Since the detection magnitude limit is affected by object crowding and background brightness level, we estimated completeness in four different regions within 1.7 R_{25} of NGC 4258, roughly at the edge of our K_s-band image ($R_{25} = 9\farcm3$ or 20.5 kpc; de Vaucouleurs et al. 1991).[4]

We explored an ellipse with semimajor axis = 0.5 R_{25}, and three elliptical annuli, respectively, from 0.5 to 1.0 R_{25}, from 1.0 to 1.4 R_{25}, and between 1.4 and 1.7 R_{25}. All 4 regions have the axis ratio and position angle (P.A.) of the observed disk of NGC 4258, i.e., 0.39 and 150°, respectively (de

[3] Different values of FLAGS indicate various problems with the photometry. For instance, sources with close bright neighbors have FLAGS = 1; blended objects, FLAGS = 2; saturated sources, FLAGS = 4.

[4] Assuming R_{25} = 13.4 kpc for the Milky Way (Goodwin et al. 1998), $\sim$ 85% of its GCs lie within 1.7 R_{25} (http://physwww.physics.mcmaster.ca/~harris/mwgc.dat).

Vaucouleurs et al. 1991). In order to estimate completeness in these four regions with statistically equivalent samples, we made sure that the added sources were inversely proportional to their area. Hence, the number of simulations considered for each region was different, respectively, 320, 106, 83, and 97.[5] On average, $\sim$ 13,300 artificial sources were added to each one of the three annuli. We will discuss the central ellipse separately below.

In the case of a box-shaped magnitude distribution, the fraction of recovered sources as a function of magnitude is well described by the Pritchet function (e.g., McLaughlin et al. 1994):

$$f(m) = \frac{1}{2}\left[1 \; - \; \frac{\alpha_{\rm cutoff}(m - m_{\rm lim})}{\sqrt{1 + \alpha^2_{\rm cutoff}(m - m_{\rm lim})^2}}\right]; \qquad (1)$$

$m_{\rm lim}$ is the magnitude at which completeness is 50%, and $\alpha_{\rm cutoff}$ determines the steepness of the cutoff.

The fraction of recovered to added sources as a function of output PSF magnitude, in bins 0.25 mag wide, was fit with equation 1 separately for each region. The values of the fit parameters $m_{\rm lim}$ and $\alpha_{\rm cutoff}$ are shown in Table 3.

In Figure 3 we display the added and recovered sources, in the left and center panels, respectively. The right panel shows the fractions of recovered to added objects vs. K_s mag, as well as the fits to them (solid lines) with eq.1.

There are some results of this completeness test that stand out: (1) the similarity between the detection magnitude limit in the K_s band data and the $m_{\rm lim}$ values in all the annuli beyond 0.5 R_{25}; (2) the brighter $m_{\rm lim}$ of the ring with the largest galactocentric distance (1.4 to 1.7 R_{25}, yellow points), compared with those of the two intermediate annuli (0.5 to 1.4 R_{25}, blue and green), and

[5] The outermost annulus spills over the borders of the image, and hence does not have the area of a complete elliptical ring.

Table 3. Completeness Fit Parameters

Region	m_{lim}	α_{cutoff}
R_{25}	K_s AB mag	
0.0 – 0.5	21.59 ± 0.01[a]	5.57 ± 0.48[a]
0.5 – 1.0	21.74 ± 0.01	14.63 ± 115.34
1.0 – 1.4	21.72 ± 0.01	8.90 ± 2.54
1.4 – 1.7	21.59 ± 0.01	3.87 ± 0.25

NOTE— [a]Errors calculated by Monte Carlo resampling, with dispersion estimated from the rms of the fit.

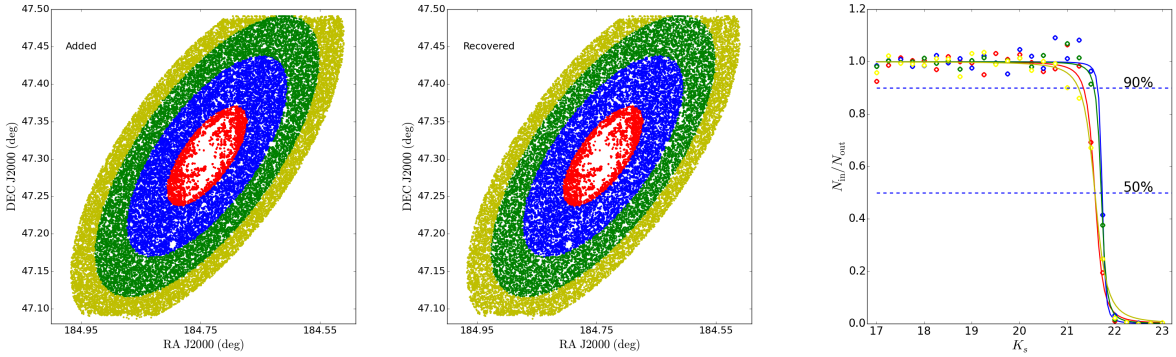

Figure 3. Completeness tests. *Left:* added sources. *Center:* recovered sources. *Right:* fits (*solid lines*) to recovered fractions (*dots*) with eq. 1. Colors (*red, blue, green, yellow*) refer to centermost ellipse, and inner, middle, and external annuli, respectively. *Blue dotted lines* indicate the 90% and 50% completeness values.

(3) the fact that there is a region close to the center where the condition to avoid overlap with real sources prevented the addition of artificial objects.

The similarity between the m_{lim} values and the source detection limit beyond 0.5 R_{25} is due to

the lack of a large low surface brightness envelope around the galaxy. In ellipticals, an envelope of completely unresolved stars results in a radial gradient of S/N that is reflected in a $m_{\rm lim}$ that likewise changes with radius.

Thus, compared to the usual case of ellipticals, the brighter $m_{\rm lim}$ in the annulus furthest away from the galaxy is counterintuitive. However, the brighter $m_{\rm lim}$ of the annulus between 1.4 and 1.7 R_{25} is a consequence of it being too close to the top and bottom edges of the image, where fewer frames contribute to the final mosaic and hence the signal-to-noise ratio is slightly smaller. We confirmed this by dividing the two most external rings in four sections, as shown in the left panel of Figure 4. The central and right panels of Figure 4 show the fit with eq. 1 to the fraction of recovered to added sources vs. K_s magnitude for the four sections, respectively, of the inner and outermost rings; the parameters of the fits are listed in Table 4.

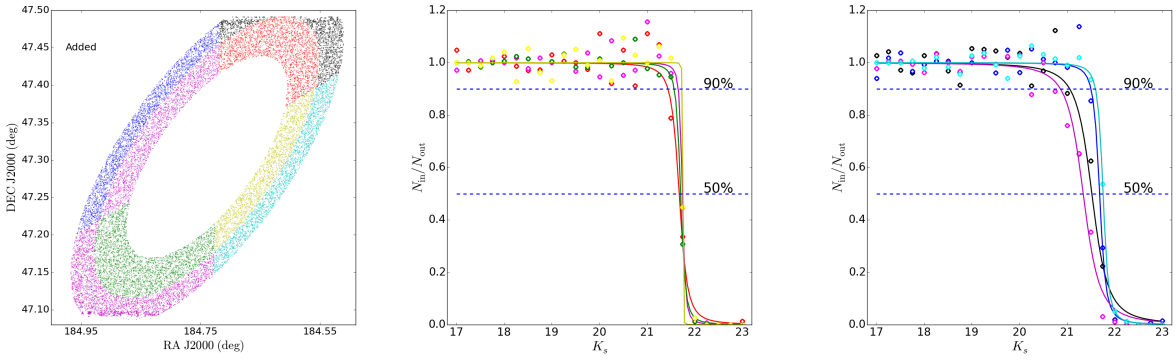

Figure 4. Completeness tests for middle and external annuli by sections. *Left:* Added sources to rings between 1.0 and 1.4 R_{25} (counterclockwise, from top, *red/north, magenta/east, green/south,* and *yellow/west*), and from 1.4 to 1.7 R_{25} (*black/north, blue/east, magenta/south, cyan/west*). *Center:* fits (*solid lines*) to recovered fractions (*dots*) in middle annulus with eq. 1. *Right:* fits to recovered fractions in external ring.

Whereas the completeness is basically the same for all four sections of the ring between 1.0 and

Table 4. Completeness Fit Parameters of Middle and External Annuli by Section

Radius R_{25}	Section Color	m_{lim} K_s AB mag	α_{cutoff}
1.0 – 1.4	Red/north	21.68 ± 0.02[a]	5.66 ± 1.34[a]
	Magenta/east	21.743 ± 0.004	15.8 ± 296.1
	Green/south	21.71 ± 0.01	9.9 ± 30.1
	Yellow/west	21.7493 ± 0.0008	146.6 ± 139.1
1.4 – 1.7	Black/north	21.52 ± 0.04	2.87 ± 0.47
	Blue/east	21.68 ± 0.02	7.40 ± 20.08
	Magenta/south	21.34 ± 0.03	2.79 ± 0.31
	Cyan/west	21.759 ± 0.005	8.39 ± 8.27

NOTE— [a]Errors calculated by Monte Carlo resampling, with dispersion estimated from the rms of the fit.

1.4 R_{25}, for the outermost annulus there is a significant difference between the top/north and bottom/south sections, on the one hand, and the left/east and right/west sections, on the other. This is consistent with our interpretation that the source detection limit in the ring between 1.4 and 1.7 R_{25} is brighter because fewer sub-integrations contribute to the final mosaic at the edges.

On the other hand, the inability to add sources in the brightest areas of the bulge and arms implies that they are strongly affected by confusion, due to partially resolved stars and star clusters. Indeed, we are not reporting the detection of any real sources there (see Figure 10), precisely because no objects have been found in those areas that are not blended or close to bright neighbors. We are aware that we have very likely missed GCCs in the brightest regions close to the center. On this

same issue, it is truly remarkable that the galactic disk between ~ 0.5 and 1 R_{25} is not having a very significant effect, neither on the addition of artificial sources nor on their recovery, compared with regions farther away from the center of the galaxy. An inspection of Figure 3 reveals that confusion should not be hampering our GCC detection beyond $\sim 0.4R_{25}$. Given the very small completeness corrections that we have derived beyond 0.5 R_{25} (and that we will duly apply in Section 7.2), the most important result of the completeness simulations is precisely this realization.

5. THE $u^*i'K_s$ DIAGRAM

Color-color diagrams are routinely used as efficient tools for the classification and selection of sources in astrophysical surveys. In particular, for GCs, examples include (r' - i') vs. (g' - i') with CFHT data (Pota et al. 2015); (F438W - F606W) vs. (F606W - F814W) with Hubble Space Telescope (*HST*) filters (Fedotov et al. 2011), and ($U - B$) vs. ($V - I$) with Very Large Telescope (VLT) images (Georgiev et al. 2006).

Recently, Muñoz et al. (2014) have shown that the combination of optical and near infrared (NIR) data into the (u^*- i') vs. (i'- K_s) color-color diagram provides the most powerful photometric only method for the selection of a clean sample of GC candidates. The $u^*i'K_s$ diagram in fact makes use of the whole spectral range between the ultraviolet (UV) and NIR atmospheric cutoffs, at 3200 $\mathring{A}$ and 2.2 μm, respectively. Thus, it samples simultaneously the main-sequence turnoff, and the red giant and horizontal branches of the stellar populations in GCs. In the $u^*i'K_s$ plane, the nearly simple stellar populations (SSPs) of GCs occupy a region that is well separated from, respectively, the loci of the composite stellar populations of background galaxies, and of foreground stars in our own Galaxy. As demonstrated also by Muñoz et al. (2014), the separation of these 3 distinct regions (i.e., GCs, galaxies, and MW stars) from the point of view of stellar populations is completely consistent with the shape parameters of the objects that inhabit them. In the case of Virgo data acquired with the

CFHT[6], sources in the galaxy region are clearly extended, those in the star band are pointlike, and many GCCs are marginally resolved.

Figure 5 presents the $u^*i'K_s$ plot for our NGC 4258 data (small solid black dots). Sources were selected by cross-matching detections by RA, DEC in our u^*, i', and K_s catalogs, with a tolerance of $1''$. The data were corrected for Galactic extinction with the Schlafly & Finkbeiner (2011) values given for the Sloan Digital Sky Survey (SDSS) filters by the NASA Extragalactic Database:[7] $A_u = 0.069$; $A_g = 0.054$; $A_r = 0.037$; $A_i = 0.028$; $A_{Ks} = 0.005$. Only data with SExtractor FLAGS=0 in all filters, and an error MAGERR_PSF < 0.2 mag in MAG_PSF in the i'-band were included. Also, since we are interested in GCs, whose luminosity function (GCLF) is practically universal, we only kept those objects within $\pm$ 3σ of the expected LF turnover (LFTO) magnitude in every filter; we assumed $\sigma = 1.2$ mag which, according to Jordán et al. (2007), is appropriate given the absolute total dereddened B mag of NGC 4258 (-20.87 mag; de Vaucouleurs et al. 1991). Values of the turnover in the optical were derived by combining the absolute TO magnitude in the g band, $M_g^0 = -7.2$ mag, for the same galaxy luminosity (Jordán et al. 2007), with the (AB) colors given in the MegaCam filter system by Bruzual & Charlot (2003, hereafter BC03) models for an SSP with $Z = 0.0004$, an age of 12 Gyr, and a Chabrier initial mass function (IMF; Chabrier 2003). The TO in the V-band would be $M_V^0 = -7.4$ mag. The TO magnitude in the K_s-band was taken from Wang et al. (2014).[8] TO absolute magnitudes, observed TO magnitudes at the distance of NGC 4258, and magnitude ranges of the GCLF are shown in Table 5.

In Figure 5, the green long-dashed line separates the cloud of background galaxies from the band

[6] Next Generation Virgo Survey (NGVS; Ferrarese et al. 2012) and NGVS-IR (Muñoz et al. 2014).

[7] The NASA/IPA Extragalactic Database (NED) is operated by the Jet Propulsion Laboratory, California Institute of Technology, under contract with the National Aeronautics and Space Administration.

[8] Wang et al. (2014) determine a TO magnitude $K_{s0} = 14.534^{+0.142}_{-0.146}$ mag for the M 31 GC system, with a Vega zero point. We apply to this value the distance modulus of Andromeda, and the transformation between Vega and WIRCam AB magnitudes (see Section 7.1).

Table 5. Turnover magnitudes and GCLF ranges

Filter	M^0	$m^0_{\rm TO}$	$m^0_{\rm TO} \pm 3\sigma$
	mag	mag	mag
u^*	-6.34	23.06	$19.46 < m^0_{u^*} < 26.66$
g'	-7.20	22.20	$18.60 < m^0_{g'} < 25.8$
r'	-7.69	21.71	$18.11 < m^0_{r'} < 25.31$
i'	-7.92	21.48	$17.88 < m^0_{i'} < 25.08$
K_s	-8.1	21.3	$17.7 < m^0_{Ks} < 24.9$

of foreground stars in the MW: objects above the line are mostly extended, sources below it are preferentially point sources, as we will show in the next subsection. The orange contour highlights the region that contains GCCs. This region was traced based on the area with the highest density of spectroscopically confirmed GCs in the $u^*i'K_s$ diagram of M 87 (Muñoz et al. 2014; Powalka et al. 2016); there are more than 2000 such sources in the GC system of M 87, and hence the GCC locus is clearly delimited. Inside the region in our plot for NGC 4258, we indicate the location of BC03 model SSPs. Each cluster of triangles represents an age sequence with a single metallicity, from $Z = 0.0004$ to $Z = 0.05$. Within each age sequence, from bluer to redder colors, models go from 8 to 12 Gyr. For illustration purposes, zero age main sequences (ZAMS) with $Z = 0.008$ and $Z = 0.02$ are shown; they sketch the locus of field stars in the MW.

Because we are interested in the GC systems of nearby spiral galaxies that are not completely edge-on, it was important to investigate the locus in the $u^*i'K_s$ plane of young stellar cluster candidates (YSCCs). The blue ellipse has been defined around BC03 models of SSPs with solar metallicity and

ages, from blue to red in (i' -K_s), between 10^7 and 10^8 yr (pink triangles). They are reasonably far away from models of old stellar populations of all metallicities. Moreover, we would like to emphasize the direction of the reddening vector in this parameter space. Although extinction could make a GC look older or more metal rich if detected through the disk of its parent galaxy, reddening would not be able to make a YSC in the disk of the galaxy look like an old GC. This is a property of the $u^*i'K_s$ diagram that makes it an ideal tool to study GC systems in spiral galaxies.

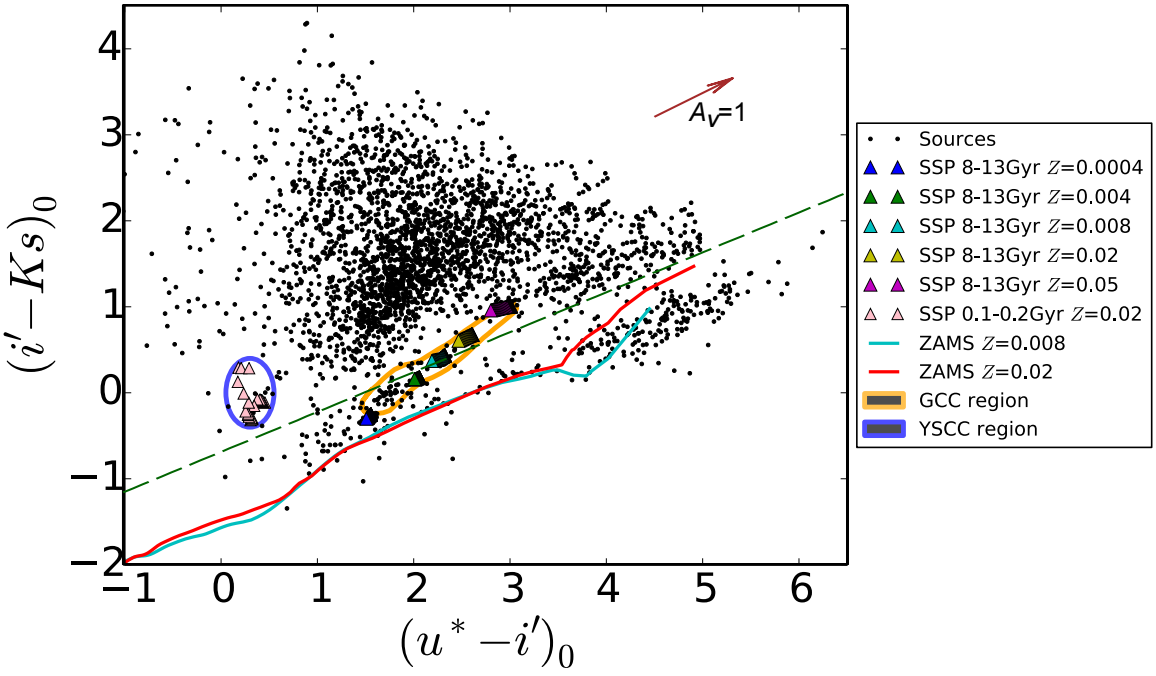

Figure 5. $u^*i'K_s$ color–color diagram of NGC 4258. *Black dots:* sources with MAGERR_PSF < 0.2 mag in the i'-band. Clusters of triangles inside the orange ellipse are age sequences, from 8 to 12 Gyr, of old SSPs with a single metallicity, i.e., *blue:* $Z = 0.0004$; *dark green:* $Z = 0.004$; *cyan:* $Z = 0.008$; *olive:* $Z = 0.02$; *purple:* $Z = 0.05$. Data points inside the orange ellipse are GCCs. *Pink triangles* inside the blue ellipse are an age sequence, from 10^7 to 10^8 yr, for an SSPs with solar metallicity; data points there are YSCCs. The *cyan* and *red* lines sketch the loci of ZAMSs with $Z = 0.008$ and $Z = 0.02$, respectively.

5.1. *Shape parameters*

Regarding the shape of the sources on the $u^*i'K_s$ plot, Figure 6 shows four different gauges of compactness in the i'-band: FWHM (top left); SPREAD_MODEL (top right); FLUX_RADIUS (bottom left); CLASS_STAR[9] (bottom right). Their values are coded as indicated by the color bars, and all of them show a correlation between locus in the color-color diagram and light concentration. Objects in the background galaxy cloud (mostly reddish-brown) are more extended than those in the Galactic star band (mostly blue), and many GCCs at the distance of NGC 4258 appear marginally resolved (cyan). Typical GC have effective radii between one and 20 pc (van den Bergh 1995; Jordán et al. 2005; Puzia et al. 2014, e.g.); one MegaCam pixel = 6.9 pc at the adopted distance to NGC 4258, and the PSF FWHM of the i' data is 0.″60 or 22 pc. In Figure 6 one can see that point sources and marginally resolved objects have FWHM $\lesssim$ 0.″8; SPREAD_MODEL < 0.015; FLUX_RADIUS $\lesssim$ 0.″5; CLASS_STAR $\gtrsim$0.4. Although not discrete, the transition value of SPREAD_MODEL between point sources and extended objects lies between $\sim$ 0.003 and 0.005, consistent with those reported by, respectively, Desai et al. (2012) and Annunziatella et al. (2013). Separation by compactness is most efficient for FWHM and SPREAD_MODEL, i.e., these parameters provide the best contrast between point sources, marginally resolved, and extended sources.

5.2. *Other diagrams*

For comparison, we show in Figure 7 color-color diagrams for the sources in the NGC 4258 field, with other combinations of CFHT filters. These are analogous to those used in works by Georgiev et al. (2006), Fedotov et al. (2011), and Pota et al. (2015). The three diagrams have many more points than our $u^*i'K_s$ diagram, since all available archival optical data are much deeper than our K_s image.

[9] The SExtractor dimensionless index CLASS_STAR is assigned by a neural network, based on the comparison between the source and the PSF. It goes from 0 for extended objects to 1 for a perfect point source (Bertin & Arnouts 1996; Hammer et al. 2010).

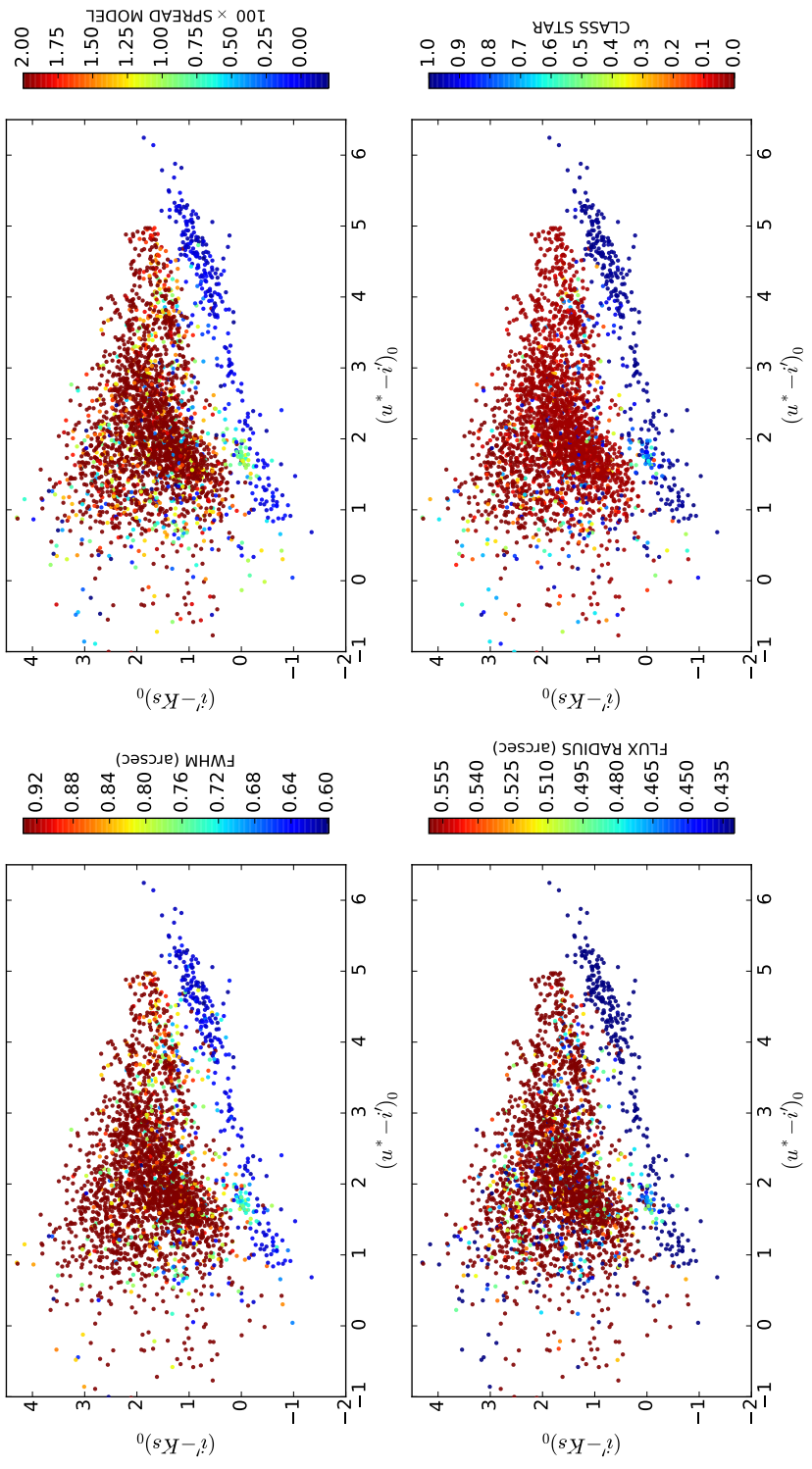

Figure 6. Morphology variations across the $u^*i'K_s$ diagram of NGC 4258. Four different indicators of shape in the i'-band, with values coded as indicated by color bars: FWHM (*top left*); SPREAD_MODEL (*top right*); FLUX_RADIUS (*bottom left*); CLASS_STAR (*bottom right*). Marginally resolved sources sport shades of cyan in all indeces.

The plots display models of young and old SSPs, as well as ZAMS, with the same ages and metallicities as in Figure 5. With the aid of the old SSP models, we have outlined with orange ellipses the expected loci of GCCs. In all cases, the contamination by background galaxies and foreground Galactic stars inside the ellipse is much more severe than with the $u^*i'K_s$ diagram. The mixture of source types in the ellipse is quite evident in Figure 8, where the shape estimators FWHM and SPREAD_MODEL in the i'-band are color-coded as previously, only for the same objects already included in Figures 5 and 6 . Both outside and within the ellipses, all ranges of light concentration can be found, rendering it questionable to select GCCs based on compactness and color-color diagram locus alone.

6. GCC FINAL SAMPLE

So far, with the aim of determining a sample of GC candidates for NGC 4258 we have imposed several restrictions: objects must have MAGERR_AUTO < 0.2 mag in the i'-band; lie within $\pm\ 3\sigma$ of the expected GCLF turnover magnitude in every filter, assuming $\sigma = 1.2$ mag; and be inside the selection region outlined in orange in the $u^*i'K_s$ color-color diagram (Figure 5).

In order to select the most likely candidates, we also rely on the shape parameters explored in the previous sections. We find that the FWHM and SPREAD_MODEL parameters calculated by SExtractor are particularly efficient in separating compact and marginally resolved sources in the selection region from more extended ones (see Figure 6). Hence, we keep sources with SPREAD_MODEL $\leqslant$ 0.017, and FWHM $\leqslant 0\farcs84$ (less than 4.5 MegaCam pixels) in the i'-band.

Given the distance to NGC 4258 (7.6 Mpc) and the angular resolution of the MegaCam data (one MegaCam pixel $= 0\farcs186 \simeq 6.9$ pc), we have likewise been able to calculate the half-light radii, r_e, in the i'-band (FWHM $= 0\farcs6 \simeq 22$ pc), of all the sources inside the selection region (outlined in orange in Figure 5) following the procedure described in Georgiev & Böker (2014). To this end, we used

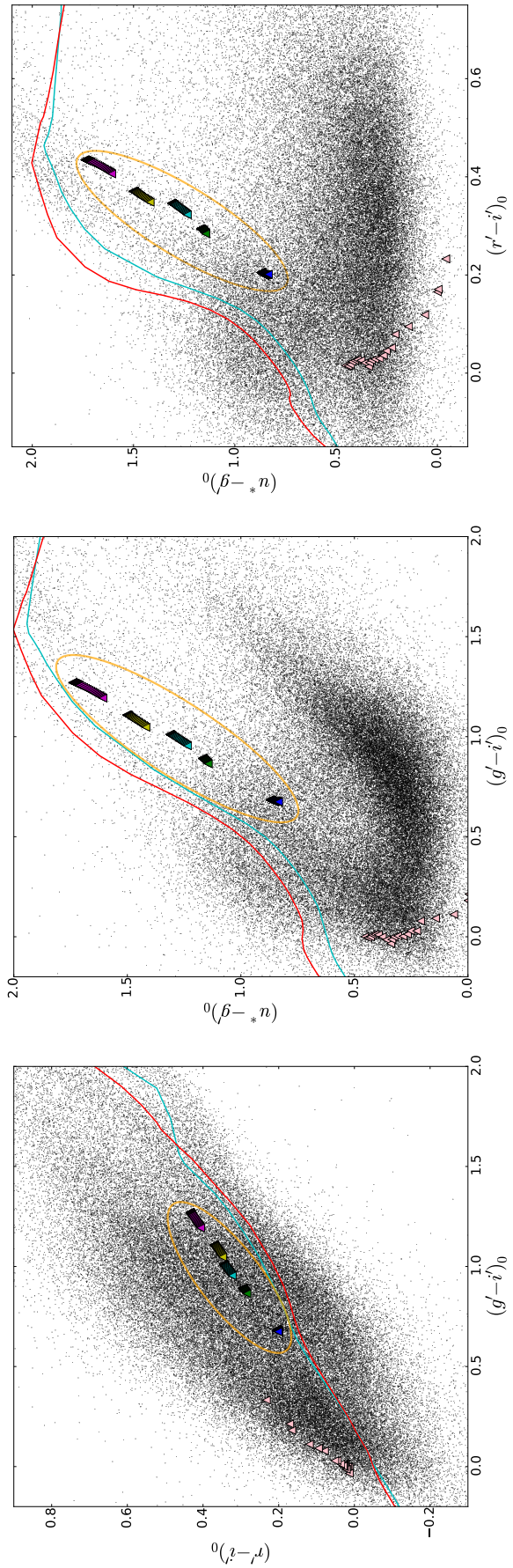

Figure 7. Alternative color-color diagrams. *Left:* $(r'$ - $i')$ vs. $(g'$ - $i')$; *middle:* $(u^*$ - $g')$ vs. $(g'$ - $i')$; *right:* $(u^*$ - $g')$ vs. $(r'$ - $i')$. Symbols for model SSPs and ZAMS as in Figure 5.

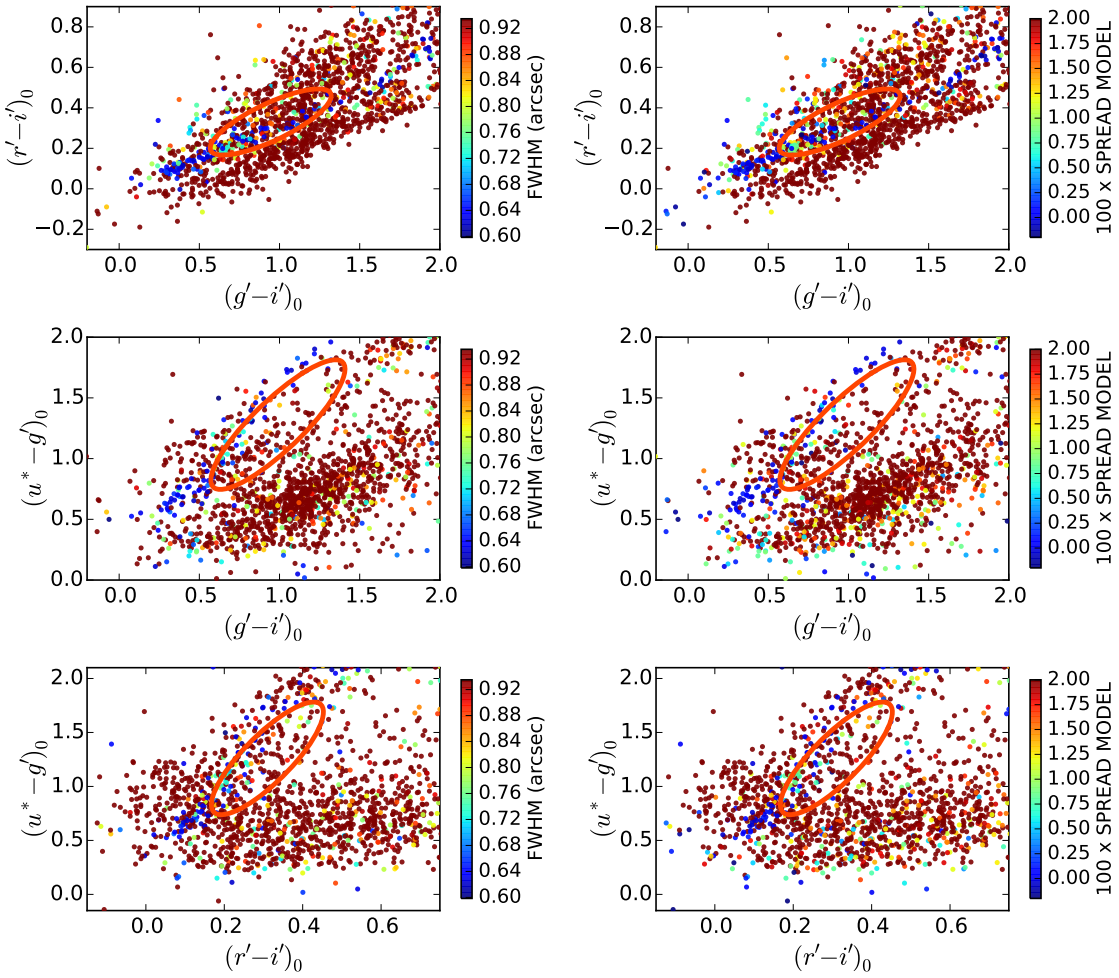

Figure 8. Morphology variations in the i'-band across alternative color-color diagrams of NGC 4258. *Top:* (r' - i') vs. (g' - i'); *middle:* (u^* - g') vs. (g' - i'); *bottom:* (u^* - g') vs. (r' - i'). *Left column:* FWHM; *right column:* SPREAD_MODEL. Orange ellipses highlight loci of GCCs; values of shape estimators coded as in Figure 6.

the program ISHAPE (Larsen 1999) in the BAOLAB[10] software package. ISHAPE measures the size of a compact source by comparing its observed light profile with a suite of model clusters, generated by convolving different analytical profiles with the image PSF. For data with S/N $\gtrsim$ 30, ISHAPE can measure $r_{\rm eff}$ reliably down to $\sim$ 0.1 the PSF FWHM, or $\sim$ 2.2 pc at the distance of NGC 4258. Objects smaller than this are effectively unresolved (Larsen 1999; Harris et al. 2009). We constructed

[10] http://baolab.astroduo.org.

a spatially variable PSF from 172 isolated stars, and we fitted all the sources with King profiles (King 1962, 1966) with fixed (KINGx) concentration indices ($C \equiv r_{\rm tidal}/r_{\rm core}$) of 30 and 100, and with the concentration index left as a free parameter (KINGn) as well. For each object, the model providing the fit to the data with the smallest χ^2 residuals was then used to derive the effective radius. This was done by applying the conversion factors between $r_{\rm eff}$ and FWHM given in the ISHAPE manual. For each source, Table 7 lists its measured r_e, the type and C index of the best-fitting King profile, the SNR of the data, and the χ^2 of the fit.

All objects left after the cuts in SPREAD_MODEL and FWHM have $r_e \leqslant 5.9$ pc. Finally, we eliminate four additional objects. One has colors, other than (u^* - i') and (i'- K_s), that are redder than the reddest BC03 model SSPS defining GCC selection regions in alternative color-color diagrams (see Section 5.2 and Figure 7); it is likely affected by dust. For three other ones, the r_e fit did not converge; one seems to be the nucleus of the dwarf galaxy SDSS J121909.07+470523.1, located to the south of NGC 4258.

Our definitive sample comprises 39 objects, all confirmed by visual inspection. Their locations in the $u^*i'K_s$ diagram are shown by the yellow points in Figure 9; the rest of the objects in the selection region are displayed in gray.

The spatial distribution is shown in Figure 10. The members of the sample are displayed as green circles on the i'-band image of NGC 4258. The dark blue ellipse outlines the region within 0.37 R_{25}, where source confusion is highest. The cyan circle indicates R_{25}. Slightly over 90% of the GCCs lie within R_{25}. We note that one object outside R_{25}, to the northwest of NGC 4258, is projected close to its companion NGC 4248, an irregular non-magellanic galaxy (de Vaucouleurs et al. 1991) with roughly the same B luminosity as the Small Magellanic Cloud. Colors and concentration parameters

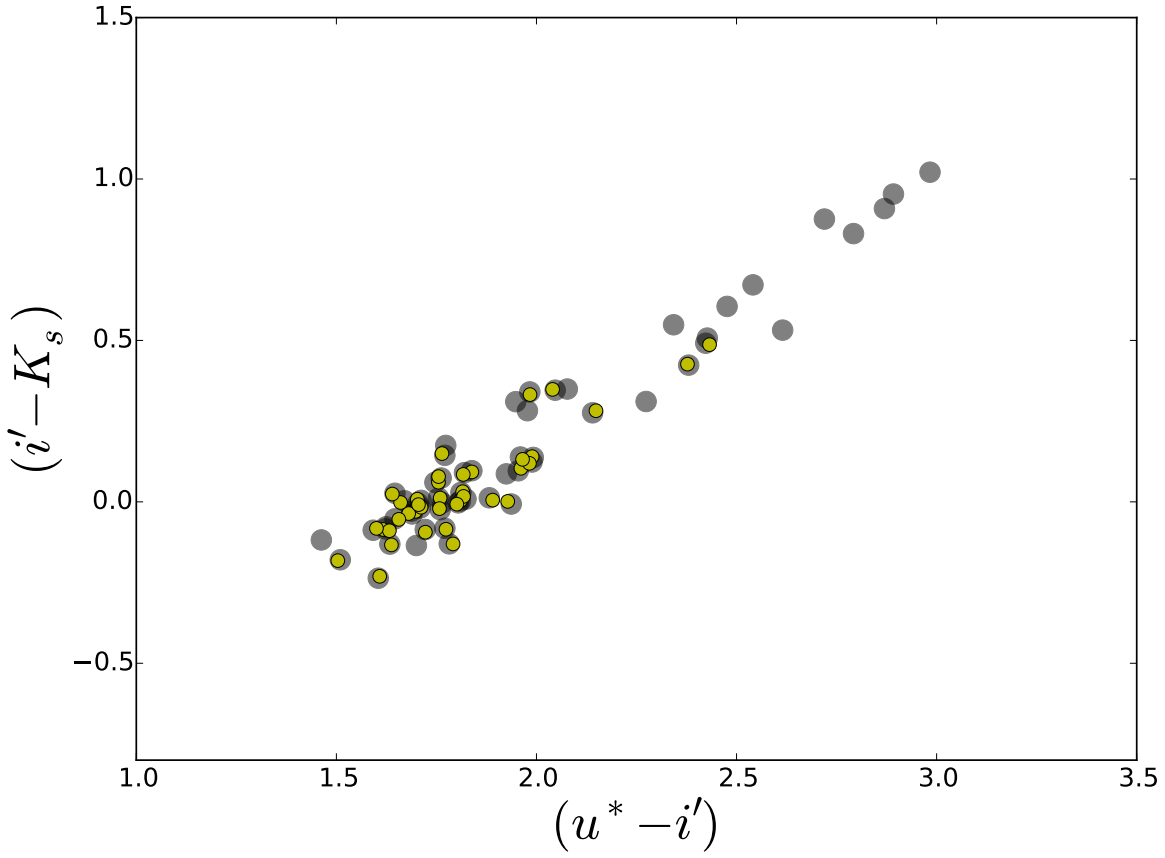

Figure 9. Location of the GCC final sample in the $u^* i' K_s$ color-color diagram. Objects in the final selection are shown as *yellow dots*. *Gray dots:* all 58 objects in the orange delimited selection region in Figure 5.
of the GCCs in the sample are given, respectively, in Table 6 and Table 7.[11]

6.1. *Decontamination*

In order to estimate the possible number of contaminants (foreground stars and background galaxies) in our sample, we use as control field CFHT observations within the Extended Groth Strip (EGS). The EGS is one of the deep fields that have been observed repeatedly in the last two decades in all the regions of the electromagnetic spectrum accessible with current technology. The original motivation to observe these fields, of which the first one was the famous Hubble Deep Field (HDF, Williams et al. 1996), is the study of the distant universe. Therefore, they are preferably at high Galactic latitudes, in order to reduce the contribution from sources in the Milky Way, and they avoid

[11] Errors in the colors are only random, and do not consider correlations between bands.

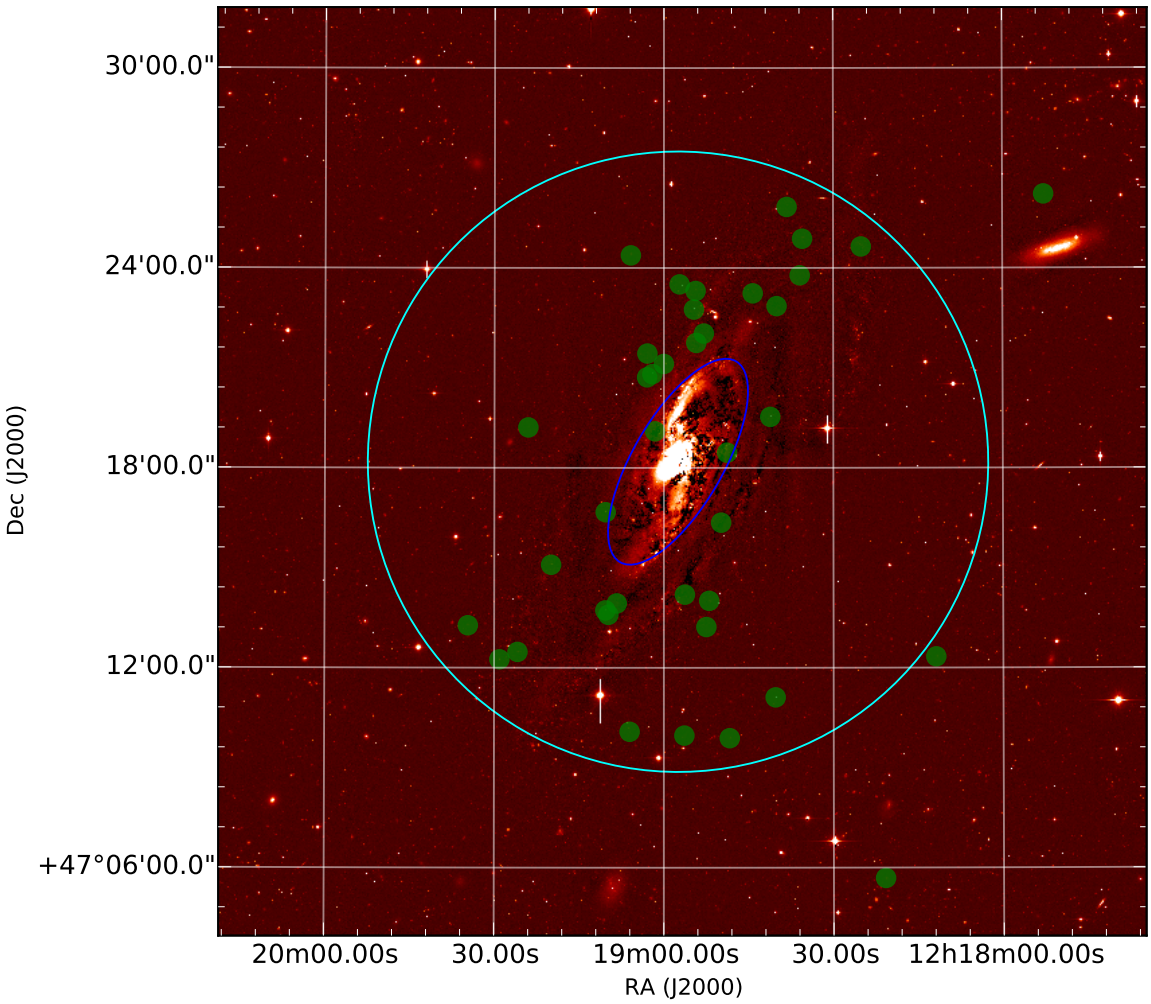

Figure 10. Spatial distribution of the GCC sample in NGC 4258. The GCCs are shown as *green filled circles*. *Dark blue ellipse:* boundary of area where source confusion is highest, with major axis = $0.37R_{25}$; *solid cyan line:* R_{25}.

lines of sight with known nearby galaxies.

The EGS is a 1.°1 by 0.°15 region located at RA = 14h19m17.84s, DEC= +52d49m26.49s (J2000), in the constellation Ursa Major. Observations of the EGS are coordinated by the All-Wavelength EGS International Survey (AEGIS; Davis et al. 2007) project. In particular, the EGS is one of the four deep fields observed by CFHT within its Legacy Survey (CFHTLS; Gwyn 2012), and the one closest to NGC 4258 in angular distance (19.°9). The D3 field of the CFHTLS consists of observations within the EGS centered at RA = 14h19m27.00s, DEC= +52d40m56s, 1 square degree in the bands u^*, g', r', i', and z', and 0.4165 square degree in J, H, and K_s. The Galactic extinction values in

Table 6. Colors of Globular Cluster Candidates

Name	RA J2000	DEC J2000	g'_0	$\Delta g'_0$	$K_{s,0}$	$\Delta K_{s,0}$	$(u^* - i')_0$	$\Delta\,(u^* - i')_0$	$(g' - r')_0$	$\Delta\,(g' - r')_0$	$(g' - i')_0$	$\Delta\,(g' - i')_0$	$(i' - K_s)_0$	$\Delta\,(i' - K_s)_0$
	deg	deg	mag	mag	mag	mag	mag	mag	mag	mag	mag	mag	mag	mag
GLL J121752+472613	184.4696	47.4370	21.686	0.006	21.08	0.16	1.690	0.009	0.443	0.009	0.646	0.007	-0.04	0.16
GLL J121811+471220	184.5494	47.2056	19.909	0.002	19.25	0.02	1.710	0.003	0.470	0.003	0.675	0.003	-0.02	0.02
GLL J121820+470541	184.5867	47.0948	19.165	0.002	18.14	0.02	1.771	0.002	0.582	0.002	0.883	0.002	0.14	0.02
GLL J121825+472438	184.6045	47.4107	20.455	0.003	19.16	0.02	1.983	0.005	0.640	0.004	0.956	0.004	0.34	0.02
GLL J121835+472452	184.6479	47.4146	19.809	0.002	19.15	0.02	1.688	0.004	0.488	0.003	0.692	0.003	-0.03	0.02
GLL J121835+472346	184.6497	47.3963	21.410	0.006	20.65	0.08	1.712	0.009	0.505	0.008	0.752	0.007	0.00	0.08
GLL J121838+472549	184.6593	47.4305	21.320	0.006	20.54	0.07	1.882	0.009	0.556	0.008	0.766	0.007	0.01	0.07
GLL J121840+472251	184.6668	47.3809	22.075	0.007	21.11	0.12	1.992	0.013	0.591	0.011	0.830	0.009	0.14	0.12
GLL J121840+471106	184.6677	47.1852	21.102	0.004	20.44	0.06	1.805	0.007	0.449	0.007	0.664	0.006	-0.00	0.06
GLL J121841+471931	184.6715	47.3255	20.653	0.003	19.94	0.04	1.746	0.005	0.467	0.005	0.656	0.004	0.06	0.04

NOTE—Table 6 is published in its entirety in the machine-readable format. A portion is shown here for guidance regarding its form and content.

Table 7. i'-Band Shape Parameters of Globular Cluster Candidates

Name	RA J2000	DEC J2000	100 ×(SPREAD_MODEL)$_{i'}$	FWHM$_{i'}$	CLASS_STAR$_{i'}$	FLUX_RADIUS$_{i'}$	$r_{e,i'}$	Shape	C index	SNR	χ^2
	deg	deg		arcsec		arcsec	pc				
GLL J121752+472613	184.4696	47.4370	0.88	0.72	0.90	0.43	$5.27^{+3.97}_{-4.13}$	KINGn	11.4	33.60	0.24
GLL J121811+471220	184.5494	47.2056	0.84	0.72	0.79	0.46	< 2.2	KINGn	289.2	168.20	2.83
GLL J121820+470541	184.5867	47.0948	0.05	0.62	0.99	0.39	$1.35^{+4.80}_{-1.32}$	KINGn	0.0	337.30	0.67
GLL J121825+472438	184.6045	47.4107	0.92	0.72	0.80	0.49	< 2.2	KINGn	635.0	142.20	2.84
GLL J121835+472452	184.6479	47.4146	1.20	0.76	0.62	0.50	$2.31^{+0.41}_{-1.70}$	KINGn	86.2	191.90	6.50
GLL J121835+472346	184.6497	47.3963	0.82	0.71	0.56	0.44	$2.64^{+0.19}_{-0.20}$	KINGx	30.0	46.90	0.37
GLL J121838+472549	184.6593	47.4305	0.78	0.72	0.95	0.44	$2.78^{+0.24}_{-0.13}$	KINGx	30.0	51.80	0.47
GLL J121840+472251	184.6668	47.3809	0.77	0.73	0.98	0.42	$5.24^{+1.81}_{-4.34}$	KINGn	12.0	28.80	0.27
GLL J121840+471106	184.6677	47.1852	0.88	0.70	0.82	0.47	< 2.2	KINGn	720.9	63.50	0.56
GLL J121841+471931	184.6715	47.3255	0.90	0.72	0.62	0.59	< 2.2	KINGx	100.0	81.20	1.06

NOTE—Table 7 is published in its entirety in the machine-readable format. A portion is shown here for guidance regarding its form and content.

this direction are $A_u = 0.037$, $A_i = 0.015$ and $A_K = 0.003$ (Schlafly & Finkbeiner 2011). All final mosaics are available in the CFHT archive,[12] and have a pixel scale of 0.″186. The exposure times of the EGS D3 CFHTLS mosaics at u^*, i', and K_s are, respectively, 19800 s, 64440 s, and 17500 s.

We remind the reader that all our analysis is limited by the K_s-band image of NGC 4258, given its FOV and shallowness. Figure 11 presents the comparison between the shape parameters of the objects in the $u^*i'K_s$ diagrams of NGC 4258 and the Groth Strip, respectively. To produce this diagram, we only include sources in an area of the EGS equal to the effective FOV of the K_s-band mosaic of NGC 4258 (612.1 arcmin^2, excluding unexposed borders), that are brighter at K_s than the limiting magnitude of the spiral galaxy data (21.7 mag). The selection region in the $u^*i'K_s$ color-color diagram is highlighted with the gray contour. The scarcity of unresolved (blue) and marginally resolved (cyan) sources within the contour in the EGS is remarkable. If we only used one parameter at a time, FLUX_RADIUS and FWHM would classify two –the same– objects as GCCs; CLASS_STAR would classify a third one, and SPREAD_MODEL would classify yet a fourth, redder one, as a GCC in the EGS field. Hence, the combination of FWHM and SPREAD_MODEL that we employed for our selection of GCCs in NGC 4258 likely allowed two contaminants to be classified as GCCs.

We adopt 2 contaminants and hence 37 as our final number of GC candidates. Incidentally, this estimate of contaminating objects coincides with the results of the very recent work by Powalka et al. (2016). They have very carefully examined, also using structural parameters, the $u^*i'K_s$ diagram of spectroscopically confirmed GCs in the M 87 field produced by Muñoz et al. (2014); Powalka et al. concluded, conservatively, that the contamination is at most 5%. Both M 87 and NGC 4258 are at high Galactic latitudes (respectively, at $b = 74.^\circ5$ and $b = 68.^\circ8$) and, indeed, the Besançon model[13] (Robin et al. 2003) predicts 8% fewer stars in the direction of NGC 4258 relative to the M 87 line of

[12] http://www.cadc-ccda.hia-iha.nrccnrc.gc.ca/en/cfht/.

[13] http://model.obs-besancon.fr/

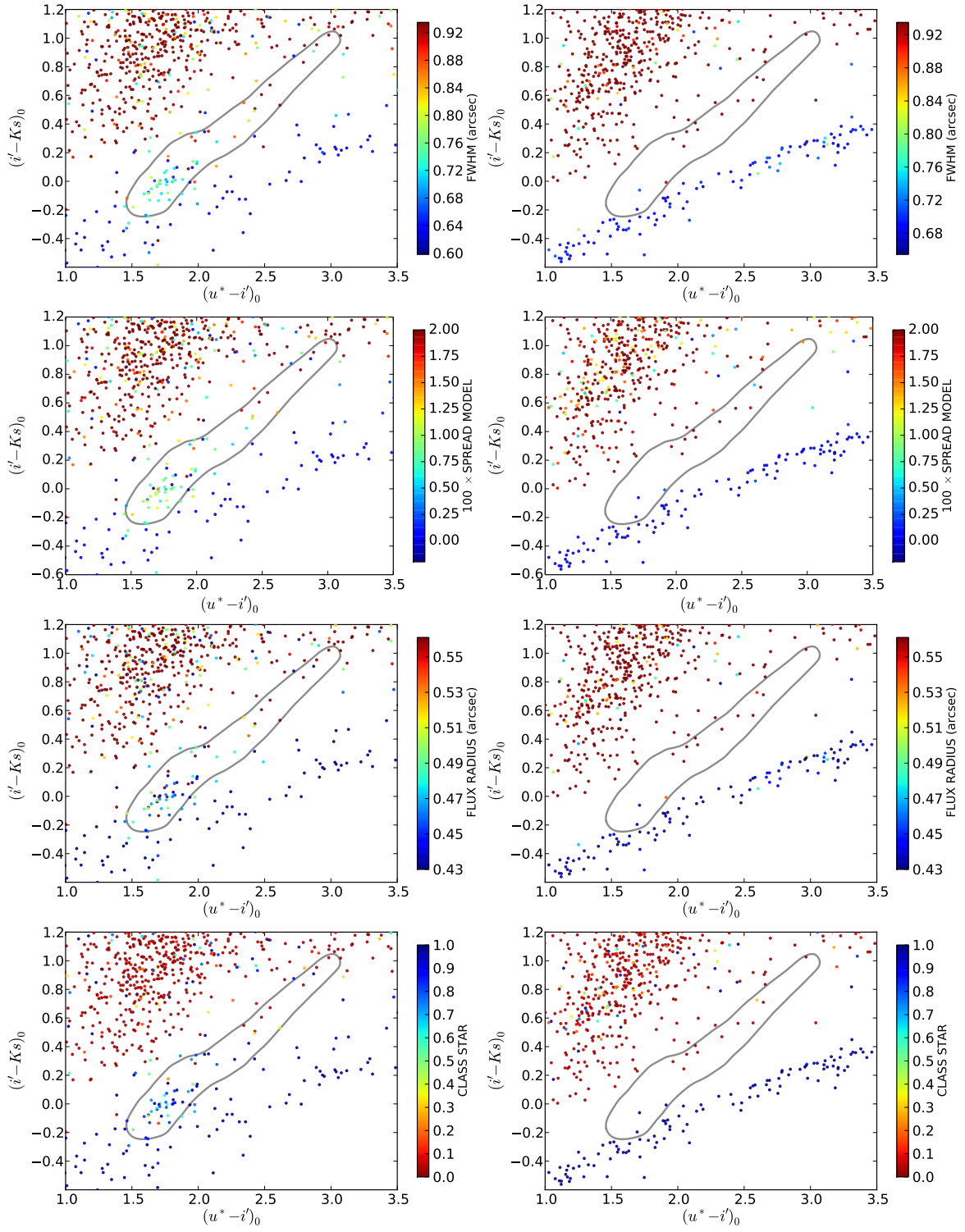

Figure 11. NGC 4258 (*left column*) and Extended Groth Strip (*right column*). Comparison of structural parameters in the GCC selection region. From *top* to *bottom:* FWHM; 100×SPREAD_MODEL; FLUX_RADIUS; CLASS_STAR. The gray contour outlines the GCC selection region. GCCs appear with shades of blue and cyan in all compactness estimators. Since the average FWHM is slightly larger for the strip mosaic than for NGC 4258 (0.″67 vs. 0.″60), we have increased accordingly the lower value of the FWHM range covered by the respective colormap. This way, point sources in the Groth Strip will show approximately with the same color as those in the NGC 4258 field.

sight.

7. PROPERTIES OF THE GC SYSTEM OF NGC 4258

7.1. *Color distribution*

The distributions of our final sample of GCCs in the colors (u^* - g'), (u^* - i'), (g' - r'), (g'- i'), (r'- i'), and (g'- K_s) are shown in the top panels of Figure 12. The colors of the individual candidates have been corrected for foreground extinction in the Milky Way, as mentioned before (Section 5). The means and dispersions of Gaussian fits to the color distributions, performed with the algorithm GMM (Muratov & Gnedin 2010), are presented in Table 8.

We now compare the colors of the GCCs of NGC 4258 with those of the globulars of our Galaxy and M 31. For the Milky Way, we use the compilation by Harris 1996 (2010 edition). This catalog comprises to date information on 147 objects, but only 82 have photometry on all $UBVRI$ bands, which we need to obtain their colors in the MegaCam system. We first transform the values in the catalog to the SDSS (AB) system with the equations in Jester et al. (2005) for stars with $R_c - I_c < 1.15$, and then to MegaCam $u^*g'r'i'z'$ magnitudes with the relations given in the MegaPipe webpage.[14] We have dereddened individually each of the 82 MW GCs using the $E(B-V)$ values in Harris 1996 (2010 edition), assuming the relative extinctions for the Landolt filter set derived by Schlegel et al. (1998) from the $R_V = 3.1$ laws of Cardelli et al. (1989, UV and IR), and O'Donnell (1994, optical).

Our transformation equations are given below, where names without superscripts refer to the SDSS system, and those with superscripts allude to the MegaCam filters:

[14] http://www.cadc-ccda.hia-iha.nrc-cnrc.gc.ca/en/megapipe/docs/filt.html.

$$u\ -g = 1.28 \times [U\ -B - 3.1 \times E(B\ -V) \times (1.664 - 1.321)] + 1.13 \quad (2)$$

$$g\ -r = 1.02 \times [B\ -V - 3.1 \times E(B\ -V) \times (1.321 - 1.020)] - 0.22 \quad (3)$$

$$g\ -i = 0.92 \times [V\ -R - 3.1 \times E(B\ -V) \times (0.819 - 0.594)] - 0.20 \quad (4)$$

$$u^* - g' = 0.759 \times (u\ -g) + 0.153 \times (g\ -r) \quad (5)$$

$$u^* - i' = 0.759 \times (u\ -g) + 1.003 \times (r\ -i) \quad (6)$$

$$g'\ -r' = 0.871 \times (g\ -r) \quad (7)$$

$$g'\ -i' = 0.847 \times (g\ -r) + 1.003 \times (r\ -i) \quad (8)$$

$$r'\ -i' = 1.003 \times (r\ -i) - 0.024 \times (g\ -r). \quad (9)$$

(u^* - g'), (u^* - i'), (g' - r'), (g'- i'), and (r'- i') color distributions of the MW globulars are shown in the middle panels of Figure 12; means and dispersions of Gaussian fits to them are also presented in Table 8.

In the case of M 31, we take the sample of *old* clusters with SDSS photometry in Peacock et al. (2010). There are 289 objects with u, g, r, and i data, as well as 173 GCs that have also been observed in the K filter with the Wide Field Camera (WFCAM) mounted on the United Kingdom Infrared Telescope (UKIRT). Whereas the optical magnitudes are given in the AB system, the infrared K values are quoted in Vega magnitudes. To transform the optical colors to the MegaCam system, we use eqs. (6)–(10). For (g' - K_s), we apply:

$$g'\ -K_s = g\ -0.153 \times (g\ -r) - K - 1.834, \quad (10)$$

where the constant 1.834 is introduced to convert K to the AB system used by WIRwolf (http://www.cfht.hawaii.edu/Instruments/Imaging/WIRCam/dietWIRCam.html). We note that Peacock et al.

(2010) have calibrated their K magnitudes with Two Micron All Sky Survey (2MASS; Skrutskie et al. 2006) K_s-band data, but the two filters are different. The K_s filter cuts off at 2.3 μm in order to reduce the contribution from the thermal background; its minimum, maximum, and central wavelengths are, respectively, $\lambda_{\rm min} = 1.95\mu$m, $\lambda_{\rm max} = 2.36\mu$m, $\lambda_{\rm cen} = 2.16\mu$m, vs. $\lambda_{\rm min} = 1.98\mu$m, $\lambda_{\rm max} = 2.47\mu$m, $\lambda_{\rm cen} = 2.23\mu$m for the K filter (http://svo2.cab.inta-csic.es/svo/theory/fps3/).

The color distributions of the M 31 old clusters are shown in the bottom panels of Figure 12, and the parameters of the Gaussian fits are listed in Table 8.

The colors reported in Peacock et al. (2010) have not been corrected for extinction, but we can estimate the reddening for the whole system as we describe below. Barmby et al. (2000) have published $UBVRI$ colors derived consistently for more than 400 M 31 clusters. Although these authors do not provide extinction corrections for their individual objects, they do find a global average reddening $E(B-V) = 0.22$. Using again the reddening law tabulations in Schlegel et al. (1998), we find $E(u^*-g') = 0.25$; $E(u^*-i') = 0.57$; $E(g'-r') = 0.19$; $E(g'-i') = 0.32$; $E(g'-K_s) = 0.68$; $E(r'-i') = 0.13$. Even without considering errors, if we correct the mean MegaCam colors of the M 31 GC system for these excesses, they are virtually identical to the colors of the MW system, as can be seen in Table 8. The redder colors of the M 31 can then be fully explained by extinction, of which about one third would be due to the relatively uncertain foreground of the MW [$E(B-V) = 0.062$; Schlegel et al. 1998], and the rest would be internal to M 31. The colors of the NGC 4258 system are slightly redder than those of the MW globulars. This small difference could also be partially due to unaccounted for internal extinction in NGC 4258.

Since in the NGC 4258 data we are 100% complete for objects brighter than the GC LFTO, we also derive colors only for the globulars in the MW and M 31 systems with $M_V \leq -7.5$ mag; for the Peacock et al. M 31 sample, we use the transformation for the SDSS filters $V = g - 0.59\times(g-r) - 0.01$ (Jester et al. 2005), and assume a distance modulus for Andromeda of 24.45 (mean and median from

NED). The colors of these subsets are likewise tabulated in Table 8, and are virtually identical to the colors of the full systems.

This brief analysis shows that, like the GCs of M 31 and our Galaxy, the GCCs in NGC 4258 do not have a bimodal color distribution, and that the colors of the three systems are remarkably consistent, once extinction has been taken into account.

7.2. *Luminosity function*

The K_s-band luminosity function for the final sample of 39 GCCs is shown in Figure 13. The histogram includes the corrections for incompleteness derived for the four different elliptical/annular regions considered in Section 4 and listed in Table 3. With these corrections, the number of sources increases to 40. The solid red line is a Gaussian fit to the histogram, with mean μ at the turnover magnitude $m^0_{\rm TO} = 21.3$, and $\sigma = 1.2$ mag. Extrapolating over the GCLF yields 65 objects.

We would like to stress here that we do not use the extrapolation over the luminosity function to derive the total number of globular clusters in the system. We perform the completeness and GCLF corrections implicitly, as we explain in the next section.

8. TOTAL NUMBER OF GLOBULAR CLUSTERS

8.1. *Correction for incomplete spatial coverage*

Usually, mostly in elliptical galaxies, the total number of globular clusters is derived from the observed sources by (1) applying the completeness correction, (2) extrapolating over the LF to account for clusters below the detection limit, and (3) accounting for incomplete spatial coverage, both due to the image FOV and to occultation/obscuration by the galaxy itself. In particular, in the case of NGC 4258, not being an edge-on spiral, it is essential to estimate the number of clusters that are lost to crowding in the brightest regions of the bulge and arms (see Section 4). Both the small number of clusters detected, and the lack of constraints in the centermost regions of the galaxy due

Table 8. Parameters of Gaussian Fits to Color Distributions

System	(u^*-g')		$(u^*-g')_0$		(u^*-i')		$(u^*-i')_0$		$(g'-r')$		$(g'-r')_0$		$(g'-i')$		$(g'-i')_0$		$(g'-K_s^a)$		$(g'-K_s^a)_0$		$(r'-i')$		$(r'-i')_0$	
	μ	σ	μ	σ	μ	σ	μ	σ	μ	σ	μ	σ	μ	σ	μ	σ	μ	σ	μ	σ	μ	σ	μ	σ
NGC 4258			1.10	0.13			1.86	0.34			0.49	0.06			0.72	0.09			0.76	0.24			0.23	0.04
Milky Way			1.03	0.15			1.67	0.25			0.45	0.09			0.64	0.11							0.19	0.03
Milky Way $M_V < -7.5$			1.02	0.15			1.65	0.25			0.45	0.09			0.64	0.11							0.18	0.03
M 31	1.30	0.26	1.05		2.29	0.53	1.72		0.64	0.17	0.45		1.00	0.28	0.68		1.24	0.61	0.56		0.36	0.12	0.23	
M 31 $M_V < -7.5$	1.30	0.26			2.29	0.52			0.64	0.17			1.00	0.28			1.23	0.59			0.36	0.11		

[a] For M 31, near-IR filter is actually K, although calibrated with the K_s-band data of the 2MASS survey. Colors of MW clusters are extinction-corrected; colors of objects in NGC 4258 are corrected for foreground Galactic extinction. For old clusters in M 31, we give uncorrected colors, and colors corrected by the average of both foreground extinction in the MW and reddening internal to M 31.

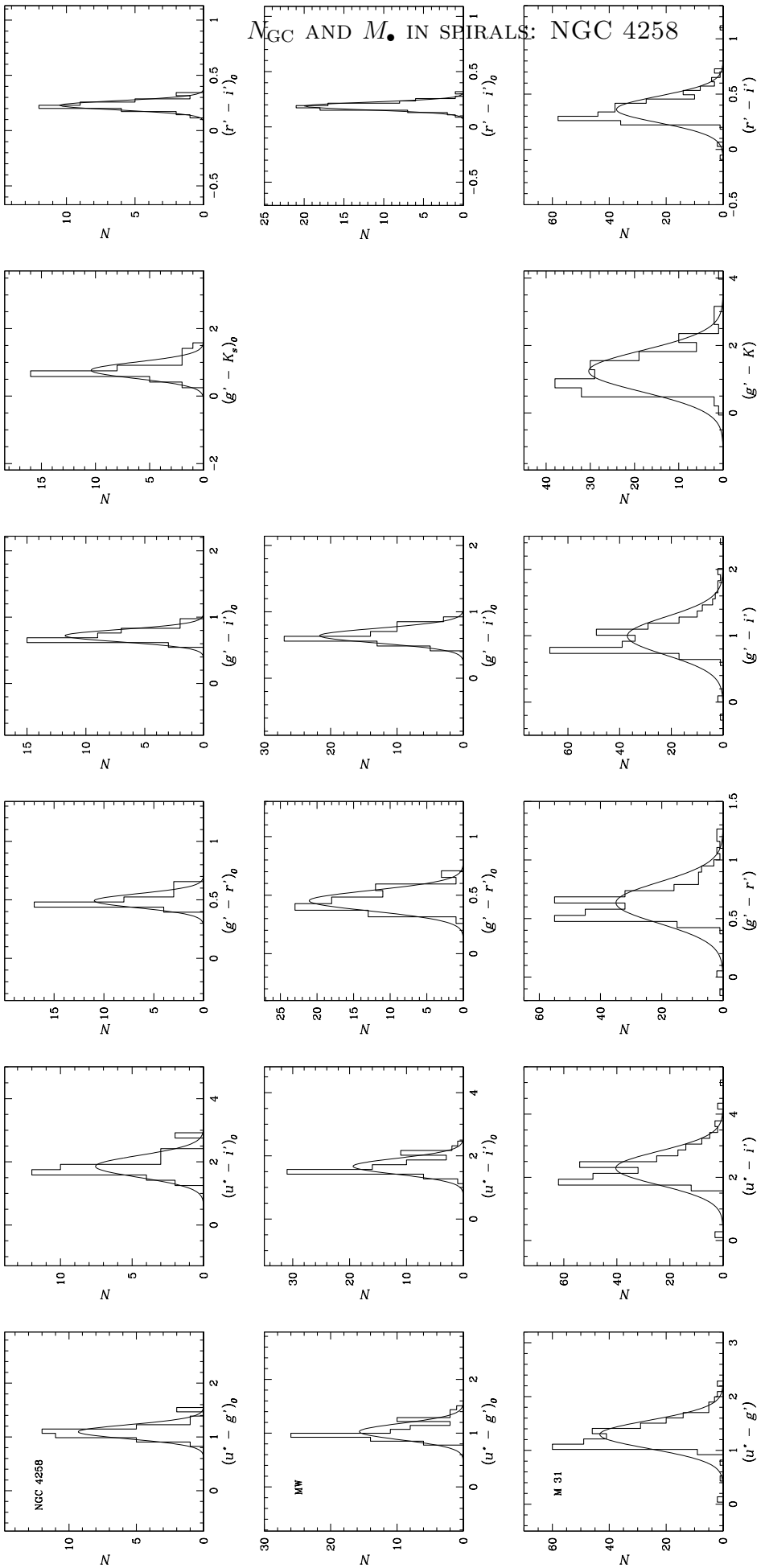

Figure 12. Color distributions of GC systems. *Top:* NGC 4258 GCCs (this work); *middle:* MW globulars (Harris 1996 2010 edition); *bottom:* M 31 old clusters (Peacock et al. 2010). From left to right: $(u^* - g')$, $(u^* - i')$, $(g' - r')$, $(g' - K_s)$, $(r' - i')$. For M 31, near-IR filter is actually K, although calibrated with the K_s-band data of the 2MASS survey.

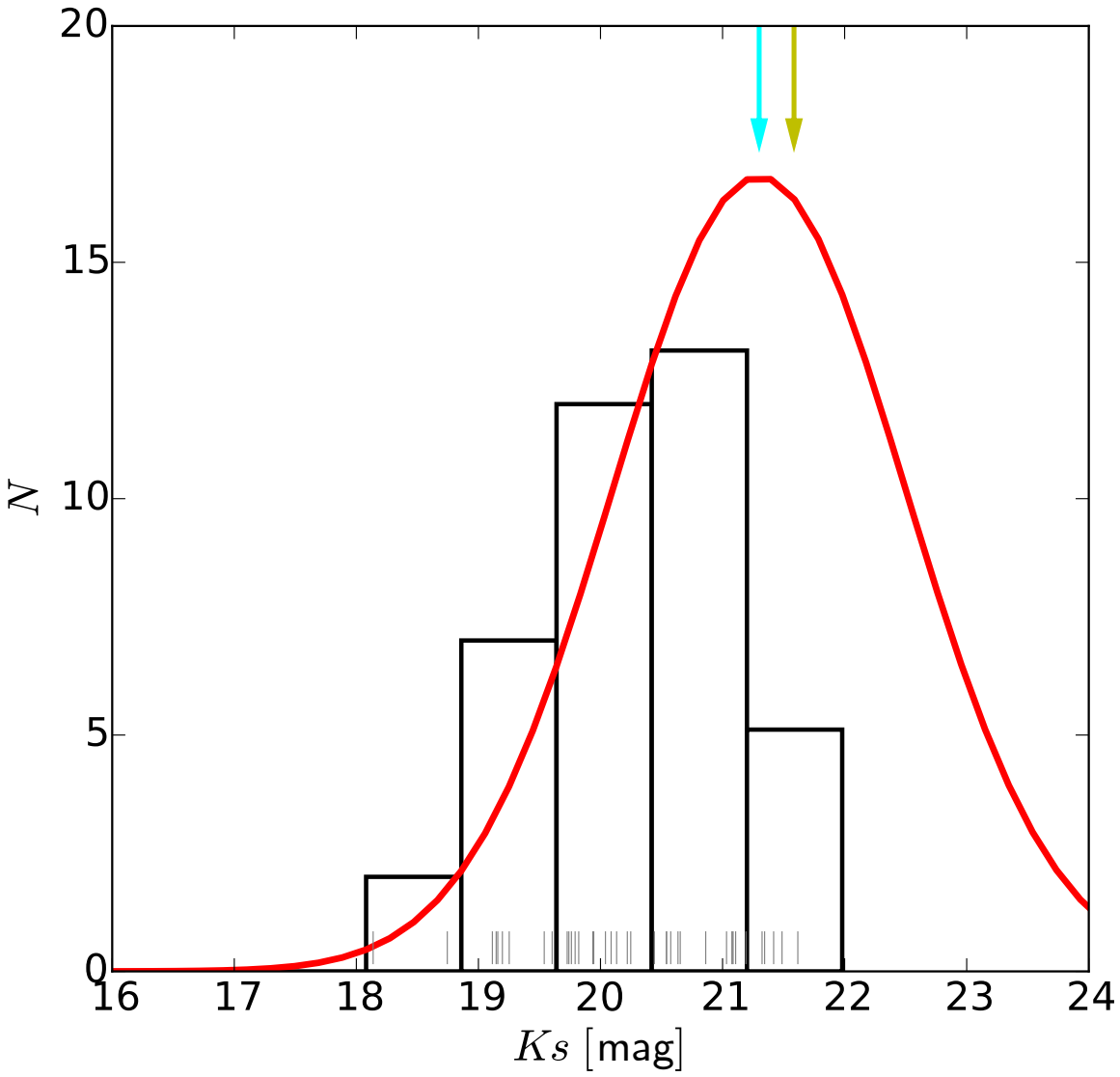

Figure 13. K_s-band luminosity function of the GCCs in NGC 4258. *Histogram:* numbers of detected objects, corrected for incompleteness using parameters derived for concentric regions (see Section 4). *Thin bars:* individual object K_s magnitudes. *Cyan arrow:* K_s TO (21.3 mag); *olive arrow:* 21.58 mag, for which completeness is 50%. *Solid red line:* Gaussian GCLF derived from fit to the corrected histogram.

to confusion prevent us from deriving this last correction from the fit to the radial distribution of GCCs customarily performed in elliptical galaxies.

Conversely, we adapt the procedure introduced by Kissler-Patig et al. (1999), based on a comparison with the GC system of the MW. With this method, the correction for incomplete spatial coverage implicitly takes care of the completeness correction and the extrapolation over the LF. Kissler-Patig

et al. (1999) and Goudfrooij et al. (2003) have discussed in detail the assumptions involved and their implications, as well as how the results are consistent with those from a fit to the radial number density, when both can be applied to the same object.

Summarizing, one estimates the number of GCs that one would detect if the MW were at the distance and orientation of the galaxy of interest, and were observed with the same instrument and to the same depth. The total number of globular clusters would then be:

$$N_{\rm GC} = N_{\rm GC}({\rm MilkyWay})\frac{N_{\rm obs}}{N_{\rm FOV}}. \quad (11)$$

$N_{\rm GC}$(Milky Way) is the total number of clusters in the MW, including objects invisible to us behind the bulge; $N_{\rm obs}$ is the number of clusters observed in the target galaxy, in our case 37 after correcting for contamination, and $N_{\rm FOV}$ is the number of objects recovered in the artificial observation of the MW. We take $N_{\rm GC}$ (Milky Way) = 160±10 (Harris et al. 2014).

In order to estimate $N_{\rm FOV}$ we use, again, the catalog by Harris 1996 (2010 edition); it provides X, Y, Z coordinates for 144 MW GCs. This coordinate system's origin is at the position of the Sun; the X axis points towards the Galactic center, the Y axis in the direction of Galactic rotation, Z is perpendicular to the Galactic plane. We define a new coordinate system $X'YZ$ with origin in the Galactic center, assuming a Galactocentric distance for the Sun R_0 = 8.34 kpc (Reid et al. 2014). The main difference with previous applications (e.g., Kissler-Patig et al. 1999; Goudfrooij et al. 2003) is that NGC 4258 is not edge-on. Hence, we have to first rotate the MW GC system in 3-D 67° with respect to the X' or Y axes, then project it on the plane of the sky; the rotated pairs $(X'_{{\rm rot},X'}, Y_{{\rm rot},X'})$, $(X'_{{\rm rot},Y}, Y_{{\rm rot},Y})$, where the subscript indicates the Galactic axis of 3-D rotation, are directly the projected coordinates. The easiest way to place the projected system on the WIRCam square FOV is to then apply a rotation around the line of sight to P.A. = 150°. We mask out an

ellipse centered on the galaxy, with semi-major axis = 3.′5, or 0.37 R_{25}, axis ratio = cos(67°), and the same P.A. of = 150° (default mask). This is the area most affected by confusion (see Section 4 and Figure 3, leftmost panel). As for the limiting magnitude, we set $V = 22.4$ mag, combining the magnitude limit at K_s with the difference between the K_s and V bands TO magnitudes; we first correct the V mag of each cluster for the Galactic extinction given in the Harris 1996 (2010 edition) catalog, and afterwards apply the foreground Galactic reddening in the direction of NGC 4258.

There are four possible orientations of the FOV and mask that preserve the alignment of the galaxy; they can be seen as mirror reflections of the projected coordinates $(+X_{\rm proj}, +Y_{\rm proj}; +X_{\rm proj}, -Y_{\rm proj}; -X_{\rm proj}, +Y_{\rm proj}; -X_{\rm proj}, -Y_{\rm proj}$, with two sets of four pairs each for rotation around the Galactic X' and Y axes, respectively). We show in Figure 14 the results of the artificial observations of the MW for the rotation around the X' and Y axes, respectively, and $+X_{\rm proj}, +Y_{\rm proj}$; angular distances in arcsec are measured relative to the center of the galaxy, with the horizontal axis increasing in the direction of decreasing RA. The ellipses delineated with the black solid line mark the outer edge of the default mask; the red crosses are clusters visible in the WIRCam FOV, whilst sources represented by black crosses have been masked out.

For the 4 realizations rotating around the X' axis we detect, respectively, 38 $(+X_{\rm proj}, +Y_{\rm proj})$, 36 $(+X_{\rm proj}, -Y_{\rm proj})$, 36 $(-X_{\rm proj}, +Y_{\rm proj})$, and 36 $(-X_{\rm proj}, -Y_{\rm proj})$ sources; for rotating around the Y axis, the numbers are 45, 46, 45, 46. We repeated the exercise with a slightly different mask for the most crowded area, i.e., an ellipse with a center displaced horizontally from the center of the galaxy 6.″45 to the east, semi-major axis = 3.′4 , axis ratio = cos(64.°5), P.A. = 153° (alternative mask); the difference was one globular cluster less detected, on average. Changing the P.A. by ±2° or the inclination angle to the line of sight, also by ±2°, had no effect.

With the numbers from the default mask, there would be 41±5 simulated MW clusters visible in NGC 4258, and eq. 11 gives for NGC 4258 a total $N_{\rm GC} = 144 \pm 31$. This error is statistical only;

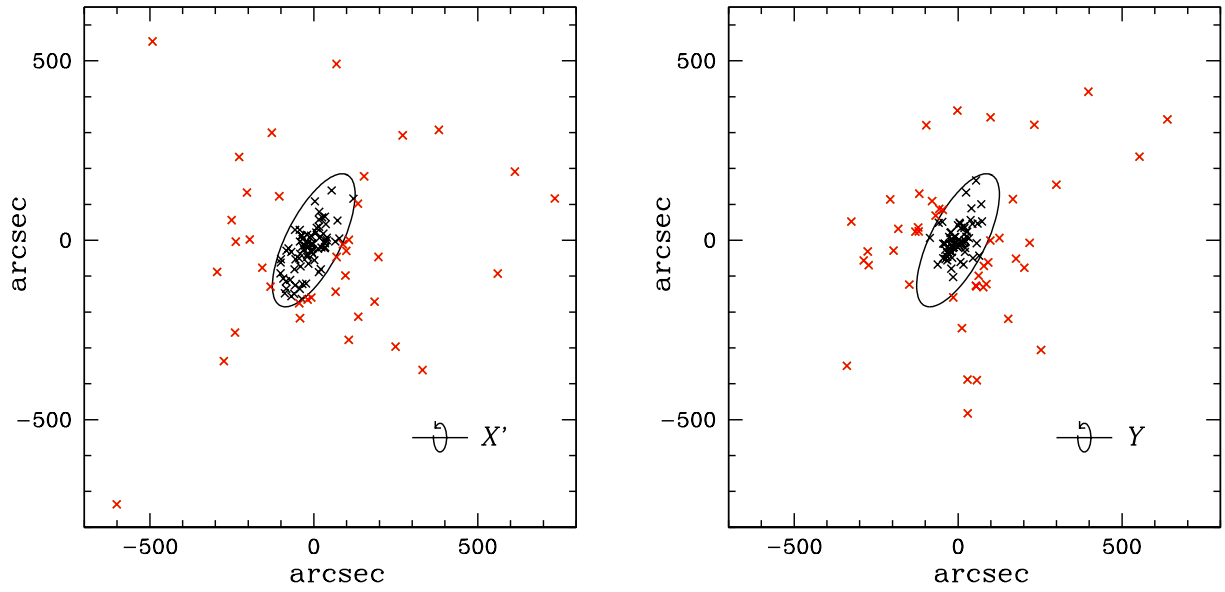

Figure 14. MW GC system, at the distance and orientation of NGC 4258. *Left:* 3-D rotation about Galactic X' axis before projection on the plane of the sky. *Right:* 3-D rotation about Galactic Y axis. *Solid black line:* default mask; *red crosses:* sources visible in the WIRCam FOV; *black crosses:* masked-out GCs.

includes errors in the assumed number of total GCs in the MW, Poisson errors in the observed number of GCCs in NGC 4258, and Poisson errors in the number of simulated clusters in the WIRCam FOV.

To this error, we add potential systematics. Errors in the distance to the galaxy result in uncertainties in the detection limiting magnitude, and in the effective areas of the galaxy covered by the FOV and excluded by the mask. For the given, rather small, uncertainties in the distance to NGC 4258 ($\pm$ 0.23 Mpc, if we add in quadrature the random and systematic errors), N_{GC} would vary by +12/-3. Another important concern is the difference in the number of obscured clusters between the MW and NGC 4258, particularly relevant, once again, because the latter is not edge-on.

Albeit with small number statistics, we performed the following experiment to try to assess the effect of dust in the galactic disk on the detection of GC candidates. We have inspected the optical images of NGC 4258 and confirmed, by the sheer numbers of background galaxies seen behind the disk beyond R_{25}, that it is quite transparent there. If the effects of dust (or crowding, for that matter) were significantly worse between 0.4 and 1 R_{25}, then we should derive a significantly larger

total number of clusters from the region outside R_{25} than from the whole field or from the area inside R_{25}. Masking out the region inside the ellipse aligned with the projected galaxy and semi-major axis = R_{25}, there are on average 15.5±0.8 simulated MW clusters, and (after correction for decontamination) 9.5 detected clusters in NGC 4258. Thus, from the outside region one would obtain 98±33 total clusters for NGC 4258, i.e., *fewer* than from the whole FOV. In view of this brief analysis, we estimate that the effect of obscuration should not be larger than a 25% variation, and that the total number of globular clusters in NGC 4258 is $N_{\rm GC} = 144\pm31^{+38}_{-36}$, with the first error statistical and the second, systematic.

We take the opportunity here to discuss the fact that the projected spatial distribution of the detected clusters in NGC 4258 appears somewhat disky/flattened. At this point, it would be hard to derive the intrinsic shape of the system, since we have a sample of only 39 objects, all outside the centermost region, and we lack kinematical information. However, we have compared the distribution of azimuthal angles ϕ of the GCCs in NGC 4258 with those of the MW projections, and also with randomly generated uniform distributions of ϕ with 39 points. The Kolmogorov-Smirnov test cannot rule out with high significance, neither that the NGC 4258 system has been drawn from a uniform distribution of azimuthal angles, nor that the MW projections and the NGC 4258 system have been drawn from the same distribution. Spectroscopic follow-up would be highly desirable to investigate whether we are looking at a large disk GC configuration. It has been reported that satellite galaxies of both the MW and M 31 may not be isotropically distributed and, instead, form coplanar groups (e.g., Metz et al. 2007, 2008, 2009; Ibata et al. 2013). Regarding in particular the MW globular clusters, two subgroups seem to have coplanar configurations (Pawlowski et al. 2012): the bulge/disk clusters, aligned with the plane of the Galaxy, and the young halo clusters (Mackey & van den Bergh 2005), at Galactocentric distances larger than 20 kpc, and lying in the same polar plane as the satellite galaxies.

9. SPECIFIC FREQUENCY, AND THE $N_{\rm GC}$ VS. $M_\bullet$ AND $M_{\rm GC}$ VS. $M_\bullet$ RELATIONS

From the distance to the galaxy, and the values of $B_{T,0} = 9.10 \pm 0.07$ mag and $(B-V)_{T,0} = 0.55$ mag given in de Vaucouleurs et al. (1991), we find $M_V = -21.42 \pm 0.10$ mag, and a specific frequency $S_N = N_{\rm GC} \times 10^{0.4\times[M_V+15]} = 0.39 \pm 0.09$, if we consider random errors only, and $S_N = 0.39 \pm 0.13$ if we include the uncertainty in the number of obscured clusters.[15] This specific frequency is comparable to the Milky Way's, which has $S_N = 0.5 \pm 0.1$ (Ashman & Zepf 1998).

Figure 15, left, displays the location of NGC 4258 (purple star) in the log $N_{\rm GC}$ vs. log $M_\bullet$ diagram, together with the Harris & Harris (2011); Harris et al. (2014) sample (ellipticals represented by solid red circles, lenticulars by open green ones). We show the random errors for NGC 4258 with purple bars, and in magenta the systematic errors added in quadrature to the former. The spiral galaxies M 31, M 81, M 104, and NGC 253 (blue crosses) fall on the elliptical correlation, the dashed line, calculated by Harris & Harris (2011) as $\log N_{\rm GC} = (-5.78 \pm 0.85) + (1.02 \pm 0.10) \log M_\bullet/M_\odot$. The MW (solid blue star), on the other hand, deviates significantly from it. For NGC 4258, the relation predicts $N_{\rm GC,predicted} = 94 \pm 14$, which we must compare with our derived $N_{\rm GC,derived} = 144 \pm 31^{+38}_{-36}$. If only random errors are considered, $N_{\rm GC,derived}$ is consistent with the prediction within 2 σ. With systematic errors added in quadrature, for 1 σ the minimum $N_{\rm GC,derived,min} = 96$, while the maximum $N_{\rm GC,predicted,max} = 108$.

We take the opportunity to include an $M_{\rm GC}$ vs. log $M_\bullet$ diagram, where $M_{\rm GC}$ is the total mass of the GC system. Burkert & Tremaine (2010) had already noticed that the total mass of the GC system is, to a good approximation, equal to the mass of the central black hole; they assumed a mean GC mass of $2\times10^5 M_\odot$, and found $M_\bullet \propto M_{\rm GC}^{1.08\pm0.04}$ for their sample. Harris & Harris (2011)

[15] The systematic error in the distance basically cancels out, because the absolute magnitude of the galaxy also changes.

speculate, however, that this equality could be coincidental and transitory, if GC systems have been continually losing mass, whereas black holes have been accreting it, since their respective births at a similar redshift.

The $M_{\rm GC}$ vs. log $M_\bullet$ for the Harris & Harris (2011); Harris et al. (2014) sample plus NGC 4258 is shown in Figure 15, right panel. $M_{\rm GC}$ values for objects in the Harris & Harris sample have been taken from Harris et al. (2013). Our fit to the ellipticals only (excluding NGC 4486B, whose SMBH mass is an upper limit) yields $\log M_{\rm GC}/M_\odot = (-1.40 \pm 0.79) + (1.15 \pm 0.09)\ \log M_\bullet/M_\odot$.

In order to place NGC 4258 in the plot, we derive the total mass of its GC system in two independent ways, and obtain the same result. (1) We calculate the dynamical mass of the galaxy as $M_{\rm dyn} = 4R_e\sigma_e^2/G$ (Wolf et al. 2010; Harris et al. 2013); $R_e = 4.6$ kpc and $\sigma_e = 115$ km s^{-1} (de Vaucouleurs et al. 1991). We then infer the mean GC mass $< M_{\rm GC} >$ from Figure 13 in Harris et al. (2013); we get $10^{5.4} M_\odot$, and multiply it by the total number of GCs that we have estimated for NGC 4258 in Section 8. The result is $\log M_{\rm GC} = 7.6 \pm 0.1 \pm 0.1$, random and systematic uncertainty, respectively, taken directly from the uncertainty in $N_{\rm GC}$. (2) On the other hand, 99% of the mass of a GC system is contained in the clusters with $M_V <$ -6.5 mag, i.e., brighter than one mag below the GCLF turnover, which is the case for all the 38 candidates we have detected. We notice (see Table 8 and Figure 12) that the (g'- r') color of the GCCs in NGC 4258, 0.49±0.06 mag, is very narrow and perfectly consistent with an SSP with age 12 Gyr, $Z = 0.0004$, and a Chabrier IMF (Bruzual & Charlot 2003). By comparing the absolute g' and r' magnitudes of our clusters with the values given by the models for one solar mass of such population, we derive their individual masses. We add them up and obtain, for both g' and r', $\log M_{\rm GC} = 7.7^{+0.3}_{-0.3}$. Here, we estimate the lower error bar assuming that the dispersion in the color distribution is due to age; an SSP with (g'- r') ~ 0.43 mag is about 5 Gyr old, and its mass-to-light ratio M/L is roughly half as for 12 Gyr. The upper error bar is dominated by the $[39\times(\frac{144}{65} - 1)]$ bright clusters that we could have missed in the crowded

region inside $\sim 0.4R_{25}$; this error would of course be smaller if the masked-out region had been more reduced, i.e., for elliptical or spiral edge-on galaxies. We show this very conservative systematic error bars in Figure 15, right panel. [16]

Since it does not depend on detecting or accounting for faint clusters, the $M_{\rm GC}$ vs. log $M_\bullet$ correlation could be a very robust way to predict $M_\bullet$ in galaxies where other methods are unavailable. Conversely, $N_{\rm GC}$ could be biased when the GCLF turnover is not reached with at least 50% completeness. The $M_{\rm GC}$ values in Harris et al. (2013) were not calculated from the brighter clusters but, rather, by adding up all clusters and assuming a mean GC mass; hence, it is not possible here to assess the intrinsic scatter of the correlation when only clusters brighter than $M_V = -6.5$ are considered. Clearly, however, this should be investigated.

10. SUMMARY AND CONCLUSIONS

Up until now, the study of GC systems in spiral galaxies has been hampered by the sparsity of their globulars, compared to ellipticals, and mostly limited to edge-on objects, given the difficulty of detecting individual GCs projected on a spiral disk. Given our goal of comparing the number of GCs vs. the mass of the SMBH in spirals, we need to study the GC systems of galaxies with measured $M_\bullet$, regardless of their orientation to the line of sight.

We have successfully applied the $u^*i'K_s$ diagram GC selection technique (Muñoz et al. 2014), for the first time to a spiral galaxy, NGC 4258. GCCs occupy a region in the $u^*i'K_s$ color-color plot that is virtually free not only of foreground Galactic stars and background galaxies, but also of young stellar clusters in the disk of the spiral galaxy of interest. We have also demonstrated, specifically for the case of NGC 4258, how superior the $u^*i'K_s$ color-color diagram is as a GCC selection tool,

[16] Taking the g and r SDSS absolute magnitudes for the Sun from http://www.ucolick.org/~cnaw/sun.html, and transforming them to the MegaCam system, we derive $(M/L)_{g'} = 3.9$, and $(M/L)_{r'} = 3.6$ for our clusters.

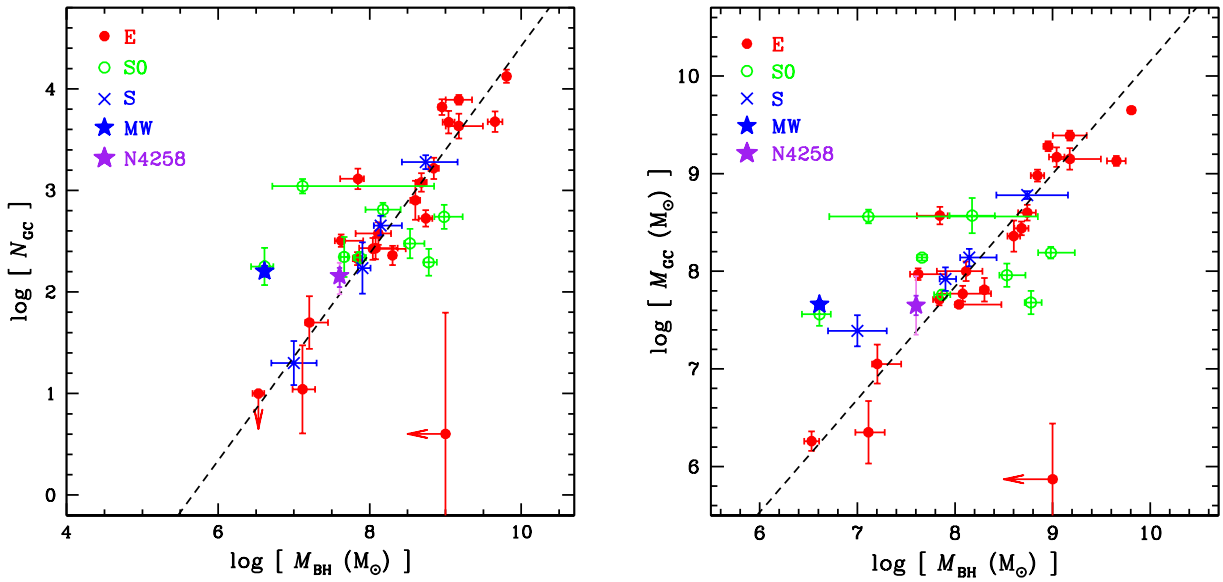

Figure 15. Relation of central black hole mass with number of globular clusters (log $N_{\rm GC}$ vs. log $M_\bullet$), *left*, and with total mass of GC system (log $M_{\rm GC}$ vs. log $M_\bullet$), *right*. Solid (*red*) and open (*green*) circles, and (*blue*) crosses represent, respectively, the elliptical, lenticular, and spiral galaxies in the sample of Harris & Harris (2011); Harris et al. (2014). The *solid blue* star is the Milky Way, also in their sample; the *solid purple* star is NGC 4258, for which we derive $N_{\rm GC}$ and $M_{\rm GC}$ in this work. The purple bars correspond to random errors only; systematic errors, added in quadrature to the former, are shown in magenta. In the log $N_{\rm GC}$ vs. log $M_\bullet$ plot, the *dashed line* is Harris & Harris's fit to the ellipticals only that are not upper or lower limits in either $N_{\rm GC}$ or $M_\bullet$. In the log $M_{\rm GC}$ vs. log $M_\bullet$ graph, the *dashed line* is our fit to the ellipticals only in the Harris & Harris sample that are not upper or lower limits in either $M_{\rm GC}$ or $M_\bullet$.

compared to other more widely used diagrams, like (r' - i') vs. (g' - i'), (F438W - F606W) vs. (F606W - F814W), and ($U\ -B$) vs. ($V\ -I$).

We complemented the $u^*i'K_s$ plot with the structural parameters (i.e., mainly effective radius r_e, FWHM, and SExtractor's SPREAD_MODEL) of the objects in the selection region to determine our final sample. We thus increased the sample of spirals with measurements of both the GC system and SMBH mass to 6 galaxies (by 20%).

The combination of the $u^*i'K_s$ diagram plus structural parameters stands as the most efficient photometric tool to investigate the GC systems in both ellipticals and spirals. Even though deep u^*/U and near-infrared images with good resolution are more expensive than optical data between

4000 and 8500 $\mathring{A}$, they are much easier to obtain than the alternative spectroscopy.

In spite of the extreme shallowness of the K_s-band data, we were able to detect 39 GCCs in NGC 4258. NGC 4258 is of special interest, since it is the archaetypical megamaser galaxy, and it harbors the central black hole with the best mass measurement outside the MW. The unimodal color distribution of the GCCs is consistent with those of the globular clusters in the MW and M 31. After completeness, GCLF, and space coverage corrections, we derive $N_{GC} = 144 \pm 31$ and $S_N = 0.4 \pm 0.1$ (random uncertainty only) for NGC 4258. The galaxy falls within 2 σ on the $N_{\rm GC}$ vs. $M_\bullet$ relation determined by elliptical galaxies. A spectroscopic study will further validate our procedures of source detection and selection; confirm the membership of our candidates in the NGC 4258 GC system; allow us determine their kinematics, the shape of the system, and the dark matter content of the halo within $\sim$ 25 kpc; investigate whether the galaxy also follows the correlation, discussed by Sadoun & Colin (2012), between $M_\bullet$ and the velocity dispersion of the GC system.

Regarding the $N_{\rm GC}$ vs. $M_\bullet$ relation for spirals, and its bearing on galaxy formation and assembly, clearly a larger sample is required. At the same time that $M_\bullet$ scaling relations have been least explored for low mass galaxies, this is precisely the mass range where different proposed scenarios could be distinguished. For example, if the ability to fuel a central black hole is correlated with a classical bulge (e.g., Hu 2008; Greene et al. 2008; Gadotti & Kauffmann 2009), then galaxies with pseudobulges could show a correlation sequence between $N_{\rm GC}$ and $M_\bullet$ that is offset towards lower MBH masses relative to the relation for ellipticals. If, on the other hand, scaling relations are determined by statistical convergence through merging (Peng 2007; Jahnke & Macciò 2011), their scatter should increase with decreasing galaxy/halo mass. Black hole masses and galaxy properties determined for low mass galaxies of varied morphologies are urgently needed, and the method we have presented here opens promising possibilities for the study of GC systems in these galaxies.

We thank the anonymous referee for her/his constructive and insightful remarks. RAGL and LL acknowledge the support from DGAPA, UNAM, through project PAPIIT IG100913; RAGL also acknowledges support from CONACyT, Mexico, through project SEP-CONACyT I0017-151671. GBA acknowledges support for this work from the National Autonomous University of México (UNAM), through grant PAPIIT IG100115. YO-B acknowledges financial support through CONICYT-Chile (grant CONICYT-PCHA/Doctorado Nacional/2014-21140651). THP acknowledges support by the FONDECYT Regular Project Grant (No. 1161817) and the BASAL Center for Astrophysics and Associated Technologies (PFB-06). Pascal Fouqué aided us to recover the information about the strategy used to observe NGC 4258 in the K_s-band with CFHT. John Blakeslee generously offered us his expertise every time we asked.

Based on observations obtained with MegaPrime/MegaCam, a joint project of CFHT and CEA/IRFU, at the Canada-France-Hawaii Telescope (CFHT) which is operated by the National Research Council (NRC) of Canada, the Institut National des Science de l'Univers of the Centre National de la Recherche Scientifique (CNRS) of France, and the University of Hawaii. This work is based in part on data products produced at Terapix available at the Canadian Astronomy Data Centre as part of the Canada-France-Hawaii Telescope Legacy Survey, a collaborative project of NRC and CNRS.

Based on observations obtained with WIRCam, a joint project of CFHT, Taiwan, Korea, Canada, France, at the Canada-France-Hawaii Telescope (CFHT) which is operated by the National Research Council (NRC) of Canada, the Institute National des Sciences de l'Univers of the Centre National de la Recherche Scientifique of France, and the University of Hawaii. This work is based in part on data products produced at TERAPIX, the WIRDS (WIRcam Deep Survey) consortium, and the Canadian Astronomy Data Centre. This research was supported by a grant from the Agence Nationale de la Recherche ANR-07-BLAN-0228

Facilities: CFHT

Software: SExtractor, PSFEx, TopCat, IRAF, Kapteyn, ISHAPE

REFERENCES

Annunziatella, M., Mercurio, A., Brescia, M., Cavuoti, S., & Longo, G. 2013, PASP, 125, 68
Ashman, K. M., & Zepf, S. E. 1998, Cambridge Astrophysics Series, 30,
Barmby, P., Huchra, J. P., Brodie, J. P., et al. 2000, AJ, 119, 727
Bertin, E. 2011, Astronomical Data Analysis Software and Systems XX, 442, 435
Bertin, E., & Arnouts, S. 1996, A&AS, 117, 393
Bruzual, G., & Charlot, S. 2003, MNRAS, 344, 1000
Boulade, O., Charlot, X., Abbon, P., et al. 2003, Proc. SPIE, 4841, 72
Burkert, A., & Tremaine, S. 2010, ApJ, 720, 516
Capuzzo-Dolcetta, R., & Donnarumma, I. 2001, MNRAS, 328, 645
Capuzzo-Dolcetta, R., & Mastrobuono-Battisti, A. 2009, A&A, 507, 183
Capuzzo-Dolcetta, R., & Vicari, A. 2005, MNRAS, 356, 899
Cardelli, J. A., Clayton, G. C., & Mathis, J. S. 1989, ApJ, 345, 245
Chabrier, G. 2003, PASP, 115, 763
Davis, M., Guhathakurta, P., Konidaris, N. P., et al. 2007, ApJL, 660, L1
Desai, S., Armstrong, R., Mohr, J. J., et al. 2012, ApJ, 757, 83
de Souza, R. S., Hilbe, J. M., Buelens, B., et al. 2015, MNRAS, 453, 1928
de Vaucouleurs, G., de Vaucouleurs, A., Corwin, H. G., Jr., et al. 1991, Third Reference Catalogue of Bright Galaxies. Volume I: Explanations and references. Volume II: Data for galaxies between 0^h and 12^h. Volume III: Data for galaxies between 12^h and 24^h., by de Vaucouleurs, G.; de Vaucouleurs, A.; Corwin, H. G., Jr.; Buta, R. J.; Paturel, G.; Fouqué, P.. Springer, New York, NY (USA), 1991, 2091 p.
Dressler, A. 1989, in IAU Symp. 134, Active Galactic Nuclei, ed. D. E. Osterbrock & J. S. Miller (Dordrecht: Kluwer), 217
Fabian, A. C. 2012, ARA&A, 50, 455
Fedotov, K., Gallagher, S. C., Konstantopoulos, I. S., et al. 2011, AJ, 142, 42
Ferrarese, L., Côté, P., Cuillandre, J.-C., et al. 2012, ApJS, 200, 4
Ferrarese, L., & Merritt, D. 2000, ApJ, 539, L9
Gadotti, D. A., & Kauffmann, G. 2009, MNRAS, 399, 621
Gebhardt, K., et al. 2000, ApJ, 539, L13
Georgiev, I. Y., Hilker, M., Puzia, T. H., et al. 2006, A&A, 452, 141
Georgiev, I. Y., & Böker, T. 2014, MNRAS, 441, 3570
Gnedin, O. Y., Ostriker, J. P., & Tremaine, S. 2014, ApJ, 785, 71
Goodwin, S. P., Gribbin, J., & Hendry, M. A. 1998, The Observatory, 118, 201
Goudfrooij, P., Strader, J., Brenneman, L., et al. 2003, MNRAS, 343, 665
Graham, A. W. 2012a, ApJ, 746, 113
———. 2012b, MNRAS, 422, 1586
Greene, J. E., Ho, L. C., & Barth, A. J. 2008, ApJ, 688, 159
Greene, J. E., et al. 2010, ApJ, 721, 26
Gültekin, K., et al. 2009, ApJ, 698, 198
Gwyn, S. D. J. 2008, PASP, 120, 212
———. 2012, AJ, 143, 38
———. 2014, Astronomical Data Analysis Software and Systems XXIII, 485, 387
Hammer, D., Verdoes Kleijn, G., Hoyos, C., et al. 2010, ApJS, 191, 143
Häring, N., & Rix, H.-W. 2004, ApJ, 604, L89
Harris, W. E. 1996, AJ, 112, 1487
Harris, G. L. H., & Harris, W. E. 2011, MNRAS, 410, 2347
Harris, W. E., Kavelaars, J. J., Hanes, D. A., Pritchet, C. J., & Baum, W. A. 2009, AJ, 137, 3314
Harris, G. L. H., Poole, G. B., & Harris, W. E. 2014, MNRAS, 438, 2117
Harris, W. E., Harris, G. L. H., & Alessi, M. 2013, ApJ, 772, 82
Herrnstein, J. R., Moran, J. M., Greenhill, L. J., et al. 1999, Nature, 400, 539
Hu, J. 2008, MNRAS, 386, 2242
Humphreys, E. M. L., Reid, M. J., Moran, J. M., Greenhill, L. J., & Argon, A. L. 2013, ApJ, 775, 13
Ibata, R. A., Lewis, G. F., Conn, A. R., et al. 2013, Nature, 493, 62
Jahnke, K., & Macciò, A. V. 2011, ApJ, 734, 92
Jalali, B., Baumgardt, H., Kissler-Patig, M., et al. 2012, A&A, 538, A19
Jester, S., Schneider, D. P., Richards, G. T., et al. 2005, AJ, 130, 873
Jordán, A., Côté, P., Blakeslee, J. P., et al. 2005, ApJ, 634, 1002
Jordán, A., McLaughlin, D. E., Côté, P., et al. 2007, ApJS, 171, 101
King, I. 1962, AJ, 67, 471
King, I. R. 1966, AJ, 71, 64
Kissler-Patig, M., Ashman, K. M., Zepf, S. E., & Freeman, K. C. 1999, AJ, 118, 197
Kormendy, J. 1993, The Nearest Active Galaxies, 197
Kormendy, J., & Gebhardt, K. 2001, 20th Texas Symposium on relativistic astrophysics, 586, 363
Kormendy, J., & Ho, L.C. (2013), ARA&A, 51, 511
Kormendy, J., & Richstone, D. 1995, ARA&A, 33, 581
Kron, R. G. 1980, ApJS, 43, 305
Laor, A. 2001, ApJ, 553, 677
Larsen, S. S. 1999, A&AS, 139, 393

Läsker, R., Ferrarese, L., van de Ven, G., & Shankar, F. 2014, ApJ, 780, 70
Läsker, R., Greene, J. E., Seth, A., et al. 2016, ApJ, 825, 3
Mackey, A. D., & van den Bergh, S. 2005, MNRAS, 360, 631
Magnier, E. A., & Cuillandre, J.-C. 2004, PASP, 116, 449
Magorrian, J., et al. 1998, AJ, 115, 2285
Marconi, A., & Hunt, L. K. 2003, ApJ, 589, L21
McLaughlin, D. E., Harris, W. E., & Hanes, D. A. 1994, ApJ, 422, 486
McLure, R. J., & Dunlop, J. S. 2002, MNRAS, 331, 795
McConnell, N. J., Ma, C.-P., Gebhardt, K., et al. 2011, Nature, 480, 215
Metz, M., Kroupa, P., & Jerjen, H. 2007, MNRAS, 374, 1125
_____. 2009, MNRAS, 394, 2223
Metz, M., Kroupa, P., & Libeskind, N. I. 2008, ApJ, 680, 287-294
Muñoz, R. P., Puzia, T. H., Lançon, A., et al. 2014, ApJS, 210, 4
Muratov, A. L., & Gnedin, O. Y. 2010, ApJ, 718, 1266
O'Donnell, J. E. 1994, ApJ, 422, 158
Oke, J. B. 1974, ApJS, 27, 21
Pawlowski, M. S., Pflamm-Altenburg, J., & Kroupa, P. 2012, MNRAS, 423, 1109
Peacock, M. B., Maccarone, T. J., Knigge, C., et al. 2010, MNRAS, 402, 803
Peng, C. Y. 2007, ApJ, 671, 1098
Pota, V., Brodie, J. P., Bridges, T., et al. 2015, MNRAS, 450, 1962
Pota, V., Graham, A. W., Forbes, D. A., et al. 2013, MNRAS, 433, 235
Powalka, M., Puzia, T. H., Lançon, A., et al. 2016, arXiv:1608.08628
Puget, P., Stadler, E., Doyon, R., et al. 2004, Proc. SPIE, 5492, 978
Puzia, T. H., Paolillo, M., Goudfrooij, P., et al. 2014, ApJ, 786, 78
Reid, M. J., Menten, K. M., Brunthaler, A., et al. 2014, ApJ, 783, 130
Rhode, K. L. 2012, AJ, 144, 154
Robin, A. C., Reylé, C., Derrière, S., & Picaud, S. 2003, A&A, 409, 523
Sadoun, R., & Colin, J. 2012, MNRAS, 426, L51
Sani, E., Marconi, A., Hunt, L. K., & Risaliti, G. 2011, MNRAS, 413, 1479
Schlafly, E. F., & Finkbeiner, D. P. 2011, ApJ, 737, 103
Schlegel, D. J., Finkbeiner, D. P., & Davis, M. 1998, ApJ, 500, 525
Silk, J., & Rees, M. J. 1998, A&A, 331, L1
Skrutskie, M. F., Cutri, R. M., Stiening, R., et al. 2006, AJ, 131, 1163
Snyder, G. F., Hopkins, P. F., & Hernquist, L. 2011, ApJL, 728, L24
Spitler, L. R., & Forbes, D. A. 2009, MNRAS, 392, L1
Terlouw, J. P., & Vogelaar, M. G. R. 2015, Kapteyn Package, version 2.3, Kapteyn Astronomical Institute, Groningen, available from http://www.astro.rug.nl/software/kapteyn/
Tremaine, S., et al. 2002, ApJ, 574, 740
Wang, S., Ma, J., Wu, Z., & Zhou, X. 2014, AJ, 148, 4
Wolf, J., Martinez, G. D., Bullock, J. S., et al. 2010, MNRAS, 406, 1220

van den Bergh, S. 1995, AJ, 110, 1171
Williams, R. E., Blacker, B., Dickinson, M., et al. 1996, AJ, 112, 1335